

# Measuring the signal strength in $t\bar{t}H$ with $H \rightarrow b\bar{b}$

Niccolo Moretti,<sup>1,\*</sup> Petar Petrov,<sup>2,†</sup> Stefano Pozzorini,<sup>1,‡</sup> and Michael Spannowsky<sup>2,§</sup>

<sup>1</sup>*Physik-Institut, Universität Zürich, Winterthurerstrasse 190, CH-8057 Zürich, Switzerland*

<sup>2</sup>*Institute for Particle Physics Phenomenology, Department of Physics,  
Durham University, DH1 3LE, United Kingdom*

A precise measurement of the Higgs boson couplings to bottom and top quarks is of paramount importance during the upcoming LHC runs. We present a comprehensive analysis for the Higgs production process in association with a semi-leptonically decaying top-quark pair and subsequent Higgs boson decay into bottom quarks. Due to the highly complex final state and large Standard Model backgrounds, measuring the signal strength in this process is known to be challenging. To maximise the sensitivity, we analyse different, statistically independent, phase space regions, where one or more of the heavy resonances are boosted. This allows us to employ jet substructure techniques, which help to reduce large  $t\bar{t} + X$  backgrounds. We find that combining several  $t\bar{t}H(b\bar{b})$  phase space regions will allow one to measure deviations of the Standard Model signal strength of order 20% with  $3\text{ ab}^{-1}$ .

## I. INTRODUCTION

After the discovery of the Higgs boson [1, 2] the precise measurement of its properties is the foremost goal during the upcoming LHC runs. All coupling measurements performed so far at 7 and 8 TeV centre-of-mass energy are in good agreement with Standard Model (SM) predictions. However, while Higgs boson couplings to gauge bosons have already been constrained in a fairly precise way [3], Higgs couplings to fermions are still plagued by large uncertainties.

Measuring Higgs couplings to bottom and top quarks is of particular importance. In the Standard Model, the bottom quark coupling drives the total width  $\Gamma_{\text{tot}}$  of the Higgs boson. When measuring the signal strength of any Higgs production and decay process  $i$ , the observed number of events depends crucially on the branching ratio,  $\text{BR}_i = \Gamma_i/\Gamma_{\text{tot}}$ , of the Higgs boson into the process-specific final state. Hence, if  $\Gamma_{\text{tot}}$  is only weakly constrained due to a large uncertainty on the Higgs-bottom coupling  $c_b$ , a precise measurement of any coupling will be hampered [4]. One way of measuring  $c_b$  is to exploit Higgs boson production in association with a gauge boson in the  $H \rightarrow b\bar{b}$  decay channel [5, 6]. This process benefits from mild combinatorial issues in the reconstruction of the two resonances, resulting in a favourable signal-to-background ratio. However, during run 1 ATLAS and CMS were only able to set weak limits on  $c_b$ , indicating the need for alternative ways to complement this measurement during the upcoming runs of the LHC [7–10].

A direct measurement of the the Higgs-top coupling  $c_t$  is desirable for several reasons: The comparatively large top quark mass, which is not explained in the Standard Model, is directly proportional to  $c_t$  and contributes in a dominant way to the destabilisation of the electroweak scale [11, 12]. An independent measurement of  $c_t$  in addition to a measurement of the Higgs self-coupling can help to evaluate if the electroweak vacuum is stable or only meta-stable on cosmological time scales. Further, many new physics scenarios predict deviations of  $c_t$  from its SM value, e.g. well-known examples include generic two Higgs-doublet models, the MSSM or composite Higgs models. While the loop-induced  $gg \rightarrow H$  and  $H \rightarrow \gamma\gamma$  processes are sensitive to  $c_t$ , direct access can only be obtained by measuring the production cross section of the Higgs boson in association with top quarks, e.g.  $t\bar{t}H$  or  $tH$ , with the former having a seven times larger cross section in the Standard Model [13–16]. Hence, for the quality of a global fit of Higgs boson properties a precise measurement of  $c_t$  through  $t\bar{t}H$  production is indispensable\*.

Both of LHC’s multipurpose experiments, ATLAS and CMS, have set limits on  $c_t$  in various channels during Run 1 [27–29]. For a light Higgs boson of 125 GeV produced in association with a  $t\bar{t}$  pair phenomenological studies have predicted sensitivity in decays of the Higgs boson to leptonic taus or  $W$  bosons [30–33], photons [34] and bottom quarks [7, 35]. Decays into leptonic taus and  $W$ s can give rise to same-sign lepton signatures which, similarly to di-photon signatures, result in a significantly improved signal-to-background ratio at the expense of a very small

\*Electronic address: moretti@physik.uzh.ch

†Electronic address: p.m.petrov@durham.ac.uk

‡Electronic address: pozzorin@physik.uzh.ch

§Electronic address: michael.spannowsky@durham.ac.uk

\*Top associated production allows to study the quantum numbers of the scalar particle using differential distributions of the decay products [17–26].

signal yield. However, while same-sign or multi-lepton signatures are unlikely to result in a narrow mass peak after reconstruction, leaving confidence in having reconstructed the  $t\bar{t}H$  final state at stake, the loop-induced  $H \rightarrow \gamma\gamma$  decay channel features a nontrivial  $c_t$  dependence that does not allow for a completely model-independent measurement of the top–Higgs coupling.

In contrast  $t\bar{t}H(b\bar{b})$  is exposed to large backgrounds but provides the largest signal yield. Consequently, the strongest constraints on  $t\bar{t}H$  production during Run 1 were obtained in this channel, where ATLAS and CMS have observed exclusion limits between 3.4 and 4.2 times the SM cross section at 95% confidence level [29, 36, 37].

As it allows to access  $c_b$  and  $c_t$  simultaneously,  $pp \rightarrow t\bar{t}H(b\bar{b})$  is one of the most important processes to measure during future LHC runs. In this paper we present a detailed study of this reaction at 14 TeV focusing on exclusive phase space regions that will become accessible at high luminosity. Earlier studies have found that going into the so-called boosted regime can improve significantly the signal-to-background ratio [7], the most limiting factor of  $t\bar{t}H(b\bar{b})$  searches<sup>†</sup>. We extend this approach using more robust signal and background calculations, employing experimentally tested taggers, and exploiting a variety of independent event topologies.

We organise this paper as follows: In Sec. II we describe in detail the event generation of signal and backgrounds. Special care is dedicated to the validation of high-statistics LO samples for  $t\bar{t}$ +multijet and  $t\bar{t} + b$ -jet production—needed for a decent description of the backgrounds in highly suppressed phase space regions—by means of NLO matched and merged simulations. After a brief overview of an early boosted analysis of  $t\bar{t}H(b\bar{b})$  in Sec. III, in Sec. IV we present alternative approaches focusing on several phase space regions in combination with a variety of reconstruction techniques. To evaluate how well the signal strength  $\mu$  can be measured for each of the aforementioned approaches we perform a binned profile likelihood test on the resulting distributions in Sec. VI. Eventually, we offer conclusions in Sec. VII.

## II. SIGNAL AND BACKGROUND CROSS SECTIONS AND EVENT GENERATION

The production of  $t\bar{t}$  pairs in association with light and heavy-flavour jets represents the dominant source of background to  $t\bar{t}H$  searches in the  $H \rightarrow b\bar{b}$  channel, and the accurate simulation of  $t\bar{t}$ +jet final states with two light or heavy-flavour jets is a key prerequisite for a reliable  $t\bar{t}H(b\bar{b})$  analysis. This calls, on the one hand, for Monte Carlo simulations based on NLO matrix elements. On the other hand, the highly exclusive cuts of the boosted analyses presented in this paper reduce the background by up to a factor  $10^{-4}$ – $10^{-5}$  with respect to the corresponding inclusive cross section. In these conditions, the production of NLO Monte Carlo samples that preserve high statistics in the signal region is very challenging. To circumvent this problem we will employ a combination of NLO and LO simulations. While the actual analysis will be based on high-statistics LO samples with appropriate dynamical scale choices and normalisation factors, NLO samples of lower statistics will be used to verify that the LO ones describe the shapes of all relevant distributions with sufficiently good accuracy. To generate the LO and NLO samples for signal and backgrounds we employ the SHERPA [40, 41] Monte Carlo<sup>‡</sup> and its built-in modules for parton showering, hadronisation, hadron decays and underlying event. Tree matrix elements are computed with AMEGIC [42] and COMIX [43], while one-loop matrix elements are generated with OPENLOOPS [44, 45] in combination with COLLIER for the evaluation of tensor integrals [46–48]. Top-quark decays are treated at LO including spin correlations based on  $t\bar{t}$ +jets Born matrix elements using spin density matrices [49, 50]. Their kinematics are adjusted a posteriori according to a Breit-Wigner distribution using the top quark width as an input.

All LO and NLO samples are generated at 14 TeV using CT10 NLO parton densities [51] and the input parameters  $m_t = 173.2$  GeV,  $M_Z = 91.1876$  GeV,  $M_W = 80.385$  GeV,  $M_H = 125.0$  GeV,  $G_\mu = 1.16675 \times 10^{-5}$  GeV<sup>-2</sup>, and  $\alpha = \sqrt{2}G_\mu M_W^2(1 - M_W^2/M_Z^2)/\pi$ . Higgs bosons are decayed in the  $b\bar{b}$  channel with branching fraction  $\text{BR}(H \rightarrow b\bar{b}) = 0.577$  [52], while the  $t\bar{t}$  system is decayed into semi-leptonic final states with NLO branching fractions  $\text{BR}(W \rightarrow q\bar{q}') = 2 \times 0.337303$  and  $\text{BR}(W \rightarrow \ell\nu) = 2 \times 0.108465$ , with  $\ell = e^\pm, \mu^\pm$ .

For the  $t\bar{t}H(b\bar{b})$  signal a NLO accurate sample is generated using the S-MC@NLO method [53, 54], which represents the SHERPA variant of the MC@NLO method [55]. Since  $H \rightarrow b\bar{b}$  decays require a non-zero bottom-quark mass, we adopt the four-flavour (4F) scheme with  $m_b = 4.75$  GeV and we use 4F CT10 parton densities. For the renormalisation ( $\mu_R$ ), factorisation ( $\mu_F$ ) and resummation ( $\mu_Q$ ) scales we choose  $\mu_R = \mu_F = \mu_Q = H_T/2 = \sum_{i=t,\bar{t},H} E_{T,i}/2$ , where  $E_T = \sqrt{p_T^2 + M^2}$ . The resulting NLO signal cross section (without decays) at 14 TeV amounts to  $\sigma_{t\bar{t}H} = 558.7(9)$  fb.

As a precise benchmark for the irreducible  $t\bar{t}b\bar{b}$  background we have performed an S-MC@NLO simulation of  $t\bar{t}b\bar{b}$  production in the 4F scheme [56]. The finite  $b$ -quark mass in the 4F scheme avoids collinear  $g \rightarrow b\bar{b}$  singularities

<sup>†</sup>Predictions for a 100 TeV hadron collider are particularly promising [38, 39].

<sup>‡</sup>More precisely we used svn revision 24881 of the SHERPA 2.1.1 public release

	$t\bar{t}b$	$t\bar{t}b\bar{b}$	$t\bar{t}b\bar{b}_{100}$
$\sigma_{\text{LO+PS}}[\text{pb}]$	8.109	1.800	0.668
$\sigma_{\text{SMC@NLO}}[\text{pb}]$	15.22	2.973	1.041
$1.65 \times \sigma_{\text{LO+PS}}/\sigma_{\text{SMC@NLO}}$	0.88	1.00	1.06

TABLE I: LO+PS and S-MC@NLO predictions for  $t\bar{t} + b$ -jet production for the subsamples with  $N_b \geq 1$  ( $t\bar{t}b$ ),  $N_b \geq 2$  ( $t\bar{t}b\bar{b}$ ) and  $N_b \geq 2$  plus an additional  $m_{b\bar{b}} > 100$  GeV cut ( $t\bar{t}b\bar{b}_{100}$ ).

and permits to cover the full  $b$ -quark phase space. Thus it provides a NLO accurate description of  $t\bar{t} + b$ -jet final states with  $b$ -jet multiplicity  $N_b \geq 1$  and  $N_b \geq 2$ . As in [56], for the factorisation and resummation scale we use  $\mu_F = \mu_Q = (E_{T,t} + E_{T,\bar{t}})/2$ , and the renormalisation scale is related to the top- and bottom-quark transverse energies by  $\mu_R^4 = \prod_{i=t,\bar{t},b,\bar{b}} E_{T,i}$ , where all transverse energies are defined at parton level.

Using the S-MC@NLO sample we have validated a high-statistics LO+PS simulation (based on the same input parameters and flavour-number scheme) that was used for the analysis in this paper. In particular, upon application of a constant  $K$ -factor we have checked that LO and NLO predictions are in decent agreement for a wide range of observables. In the following we present comparisons of LO and NLO predictions that have been obtained by switching off top-quark decays, hadronisation and underlying event. This approach, allows one to focus on those jets that originate from QCD interactions and are most sensitive to NLO corrections. In Table I we compare LO+PS and S-MC@NLO predictions for  $t\bar{t} + b$ -jet cross sections with a different number,  $N_b$ , of  $b$ -jets<sup>§</sup> with  $p_T > 25$  GeV and  $|\eta| < 2.5$ . The inclusive case with  $N_b \geq 1$  (denoted as  $t\bar{t}b$ ) is compared to more inclusive cross sections with  $N_b \geq 2$  ( $t\bar{t}b\bar{b}$ ) and  $N_b \geq 2$  plus an additional cut,  $m_{b\bar{b}} > 100$  GeV, on the invariant mass of the first two  $b$ -jets ( $t\bar{t}b\bar{b}_{100}$ ). In the actual analysis the LO+PS  $t\bar{t}b\bar{b}$  simulation is improved by a constant  $K$ -factor of 1.65. As can be seen from Table I, this reduces the discrepancy between LO+PS and S-MC@NLO predictions to about 10% or less in the three considered subsamples, while the intrinsic scale uncertainty of the S-MC@NLO prediction is around 20–30% [56]. We have checked that such good agreement between rescaled LO+PS and S-MC@NLO predictions holds also for a number of distributions. This is illustrated in Figure 1 for various observables in the  $t\bar{t}b$  and  $t\bar{t}b\bar{b}$  subsamples. The largest discrepancies do not exceed 20% and are observed in phase space regions that are not critical for a boosted  $t\bar{t}H(b\bar{b})$  analysis, such as in the region of large  $\Delta R_{b\bar{b}}$ . In contrast, for the most relevant observables, such as the  $p_T$  and invariant-mass distributions of the  $b$ -jets, the observed deviations between LO and NLO predictions are well below the intrinsic S-MC@NLO uncertainty.

As a benchmark for  $t\bar{t}$ +multi-jet production we have produced an inclusive sample based on the MEPS@NLO technique [57, 58]. In this approach, S-MC@NLO simulations of  $t\bar{t} + n$ -jet production with  $n = 0, 1, \dots, n_{\text{max}}$  are consistently merged to form an inclusive sample that provides an NLO accurate description of any observable involving up to  $n_{\text{max}}$  jets. First applications of NLO merging techniques to  $t\bar{t}$ +multijet production have been presented in [59, 60] for  $n_{\text{max}} = 1$  and in [61] for  $n_{\text{max}} = 2$ . Given the high computational cost of handling  $t\bar{t} + 2$  jet final states at NLO, in this study we will restrict ourselves to a MEPS@NLO simulation for  $t\bar{t} + 0, 1$  jets. As in [61], for the  $pp \rightarrow t\bar{t}$  core process we choose the scales  $\mu_R = \mu_F = \mu_Q = \mu_{\text{core}}$  with  $1/\mu_{\text{core}}^2 = 1/\hat{s} + 1/(m_t^2 - \hat{t}) + 1/(m_t^2 - \hat{u})$ , while the scale of the  $\alpha_S$  factors associated with additional jet emissions is set equal to the transverse momentum of the corresponding branchings. The latter are determined in a probabilistic way by inverting the SHERPA parton shower. For the separation of the  $t\bar{t} + 0$ -jet and  $t\bar{t} + 1$ -jet S-MC@NLO samples the merging scale  $Q_{\text{cut}} = 30$  GeV is used.

Heavy quarks are described in the massless approximation using the five-flavour (5F) scheme with CT10 5F PDFs. Double counting with the (N)LO matched  $t\bar{t}b\bar{b}$  sample in the 4F scheme is avoided by vetoing final states with one or more  $b$ -quarks in the (N)LO merged 5F simulation. In particular, also  $t\bar{t} + b$  configurations with a single  $b$ -quark need to be vetoed since they are already taken into account in the 4F scheme through  $gg \rightarrow t\bar{t}b\bar{b}$  subprocesses where one of the  $b$ -quarks remains unresolved in initial-state  $g \rightarrow b\bar{b}$  collinear splittings.

Since  $b$ -production takes place both through matrix elements and parton showers, the matching of 4F  $t\bar{t}b\bar{b}$  production and 5F  $t\bar{t}$ +jets production needs to be based on a  $b$ -quark veto after parton showering. However,  $b$ -quarks that arise from the decay of top quarks (and their subsequent showering) in  $t\bar{t}$ +light-jet events are not vetoed since such configurations cannot arise from  $t\bar{t}b\bar{b}$  4F matrix elements.

Similarly as for the  $t\bar{t}b\bar{b}$  simulations, also for the inclusive  $t\bar{t}$ +jets background our analysis relies on a high-statistics LO sample. More precisely, using the same scale choices as for MEPS@NLO, we have generated a MEPS@LO  $t\bar{t} + 0, 1, 2$  jets sample, with up to two jets at matrix-element level. Again, thanks to the adopted scale choices and

<sup>§</sup>For these technical comparisons we use the anti- $k_T$  algorithm with  $R = 0.4$  and we define as  $b$ -jets those jets that contain one or more  $b$ -quarks among their constituents.

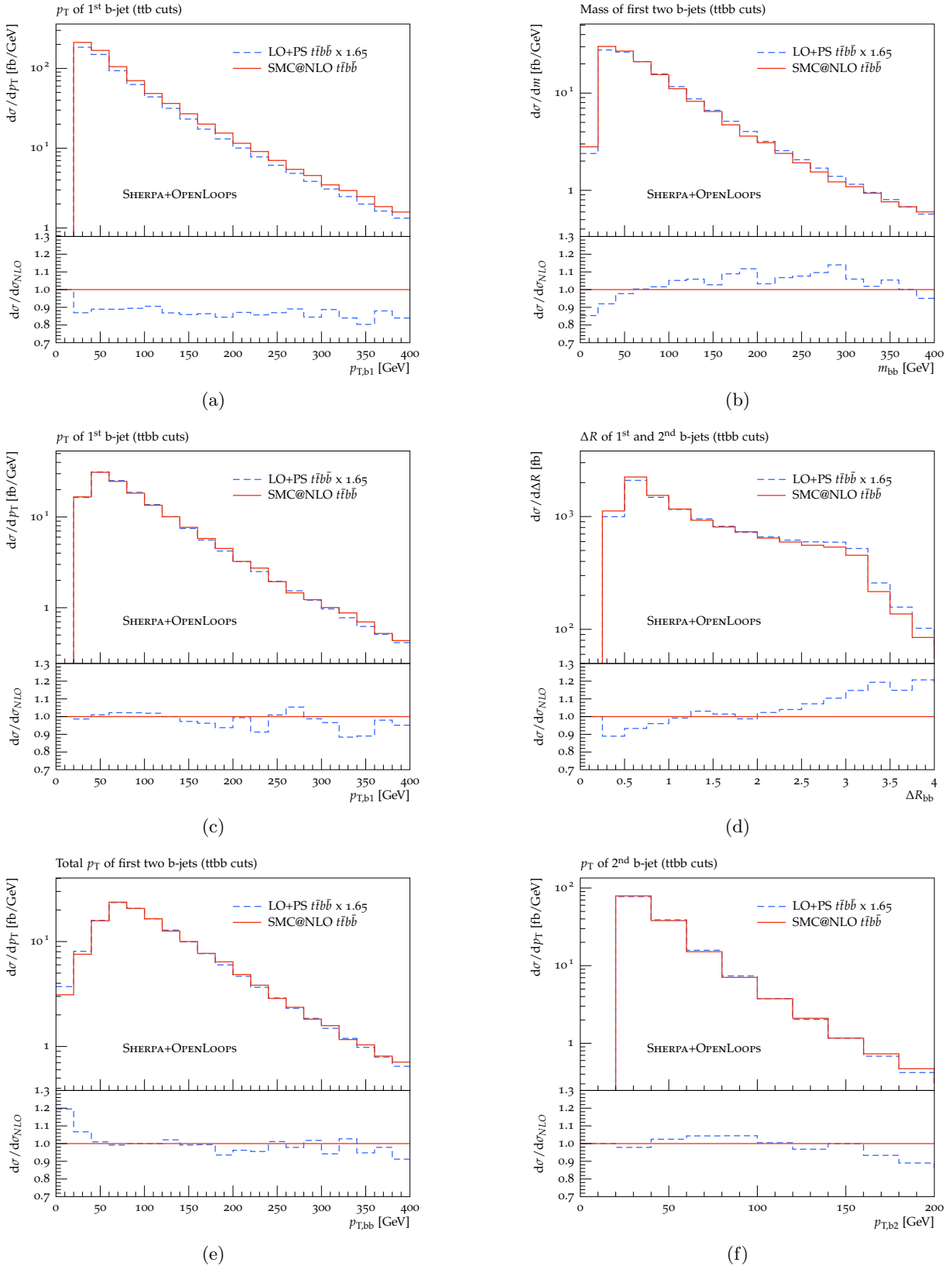


FIG. 1: Comparison of LO+PS and S-MC@NLO predictions for  $p_T$  of first  $b$ -jet in the inclusive  $ttb\bar{b}$  subsample (1a) and various observables in the  $ttb\bar{b}$  subsample: invariant mass of first two  $b$ -jets (1b),  $p_T$  of first  $b$ -jet (1c),  $\Delta R$  of first two  $b$ -jets (1d), total  $p_T$  of first two  $b$ -jets (1e) and  $p_T$  of second  $b$ -jet (1f). In this comparison top decays, hadronisation and underlying event are switched off. A constant  $K$ -factor of 1.65 is applied to the LO+PS  $ttb\bar{b}$  simulation.

	$t\bar{t} + \geq 0 \text{ jets}$	$t\bar{t} + \geq 1 \text{ jets}$	$t\bar{t} + \geq 2 \text{ jets}$	$t\bar{t} + \geq 3 \text{ jets}$
$\sigma_{\text{MEPS@LO}} [\text{pb}]$	506.8	268.3	113.0	42.66
$\sigma_{\text{MEPS@NLO}} [\text{pb}]$	790.9	419.3	175.5	65.00
$1.559 \times \sigma_{\text{MEPS@LO}} / \sigma_{\text{MEPS@NLO}}$	1.000	1.002	0.996	0.977

TABLE II: MEPS@LO and MEPS@NLO predictions for  $t\bar{t}$ +multijet production in jet bins. Top quarks are kept stable, and the jet counting refers to generic (light or heavy-flavour) jets.

an appropriate  $K$  factor, LO and NLO predictions turn out to be in good agreement. Cross sections for  $pp \rightarrow t\bar{t} + 0, 1, 2, 3 \text{ jets}$  are compared in Table II, using an anti- $k_T$  jet algorithm with  $R = 0.4$  and counting jets with  $p_T > 25 \text{ GeV}$  and  $|\eta| < 2.5$ . Applying a constant  $K$ -factor of 1.559 brings MEPS@LO and MEPS@NLO in striking agreement for all considered jet multiplicities. We also compared the MEPS@LO simulation rescaled with  $K = 1.559$  to fixed-order NLO calculations for  $t\bar{t} + 1 \text{ jet}$  and  $t\bar{t} + 2 \text{ jet}$  production [62, 63]. For the respective cross sections with one and two jets with  $p_T > 50 \text{ GeV}$  we found agreement within 5% or so, i.e. below the level of uncertainty expected from NLO scale variations. In the final analysis the inclusive  $t\bar{t}$  sample is normalised to the NNLO+NNLL result  $\sigma_{t\bar{t}} = 956.2 \text{ pb}$  [64], which corresponds to applying an overall  $K$ -factor of  $1.209 \times 1.559 = 1.885$  to the MEPS@LO sample. The comparison of differential observables presented in Figure 2 demonstrates that in MEPS@LO approximation also the shape of the most important variables is sufficiently well described. The observed shape differences between MEPS@LO and MEPS@NLO predictions approach 10% only in the hard tails of the jet- $p_T$  distributions.

In summary we are going to use an S-MC@NLO signal sample, a LO+PS  $t\bar{t}b\bar{b}$  sample and a  $t\bar{t} + 0, 1, 2 \text{ jet}$  merged sample based on the MEPS technique at LO. As discussed above, the background samples have been rescaled with appropriate  $K$ -factors and validated by means of S-MC@NLO and MEPS@NLO simulations. The overlap between the  $t\bar{t}b\bar{b}$  and  $t\bar{t}$ +multijet samples is consistently removed by vetoing any  $t\bar{t}$ +multijet event containing  $b$ -quarks that do not originate from (showered) top quark-decays.

### III. STANDARD BOOSTED $t\bar{t}H$ ANALYSIS

In this paper we focus on the extraction of the  $t\bar{t}H(b\bar{b})$  signal at the 14 TeV LHC in the semi-leptonic channel. As a starting point of our study, in this section we will consider a standard boosted analysis along the lines of [7]. While following the general strategy of [7], as detailed below we will introduce a first series of simple improvements, such as the usage of the HEPTopTagger, as proposed in [65], updated reconstruction approaches, lepton isolation requirements, more reliable treatment of  $B$ -mesons and so on. Moreover the accuracy of Monte Carlo simulations for signal and backgrounds will be upgraded from LO to NLO, with a significant impact on the expected sensitivity. A major extension of the boosted approach, including completely new regions of phase space, will be introduced in Sec. IV.

The strategy proposed in [7], in order to improve the separation of the  $t\bar{t}H(b\bar{b})$  signal from the problematic QCD backgrounds of type  $t\bar{t} + X$  and  $W + \text{jets}$ , exploits final states where both the hadronically decaying top,  $t_{\text{had}}$ , and the Higgs boson are modestly boosted ( $p_T \gtrsim m$ ) and balance each other's transverse momenta, so that their decay products tend to occupy different physical regions of the detector.

The boosted selection processes three types of Monte Carlo (MC) objects: *hadrons*, *leptons* and  *$B$ -mesons*. For leptons,  $\ell = e^\pm$  or  $\mu^\pm$ , we require  $|\eta_\ell| < 2.5$  and  $p_{T\ell} > 25 \text{ GeV}$ , following [36], and impose the lepton isolation requirement  $\sum_{i \in \Delta R_{i\ell} < 0.2} H_{Ti} < 0.1 p_{T\ell}$ . All other visible final state particles with  $p_T > 0.5 \text{ GeV}$  and  $|\eta| < 4.5$  are treated as hadrons. While  $B$ -mesons were kept stable in [7], the present analysis includes  $B$ -decays and resulting  $b$ -jet energy losses in case of semi-leptonic  $B$ -decays (see more details in Sec. V). However a simplified  $b$ -tagging modelling based on  $B$ -mesons before decays is used. For a jet or subjet to be labelled as  $b$ -jet, a  $B$ -meson with  $p_T > 10 \text{ GeV}$  and  $|\eta| < 2.5$  before decay has to fall within the jet radius ( $\Delta R_{B,\text{jet}} < R_{\text{jet}}$ ). When all jets and subjets in a configuration are MC-tagged as  $b$ -jets or light jets, a  $b$ -tag weight is given to the configuration as a whole by calculating the probability of a specific number of  $b$ -jets and light jets based on 70% and 1% tagging efficiencies for  $b$ -jets and light (or charm) jets, respectively. All jets that lie outside the rapidity region  $|y| < 2.5$  are tagged as light jets.

Similarly as in [7], two preselection cuts are applied in order to suppress the overwhelming QCD background. First, we require exactly one isolated charged lepton in the event. Since an isolated lepton is produced in the hard process and not in subsequent hadron decays, this condition makes the pure multi-jet background insignificant and also separates the semi-leptonic  $t\bar{t} + X$  decay channels from the fully leptonic ones. Second, the *hadrons* are clustered

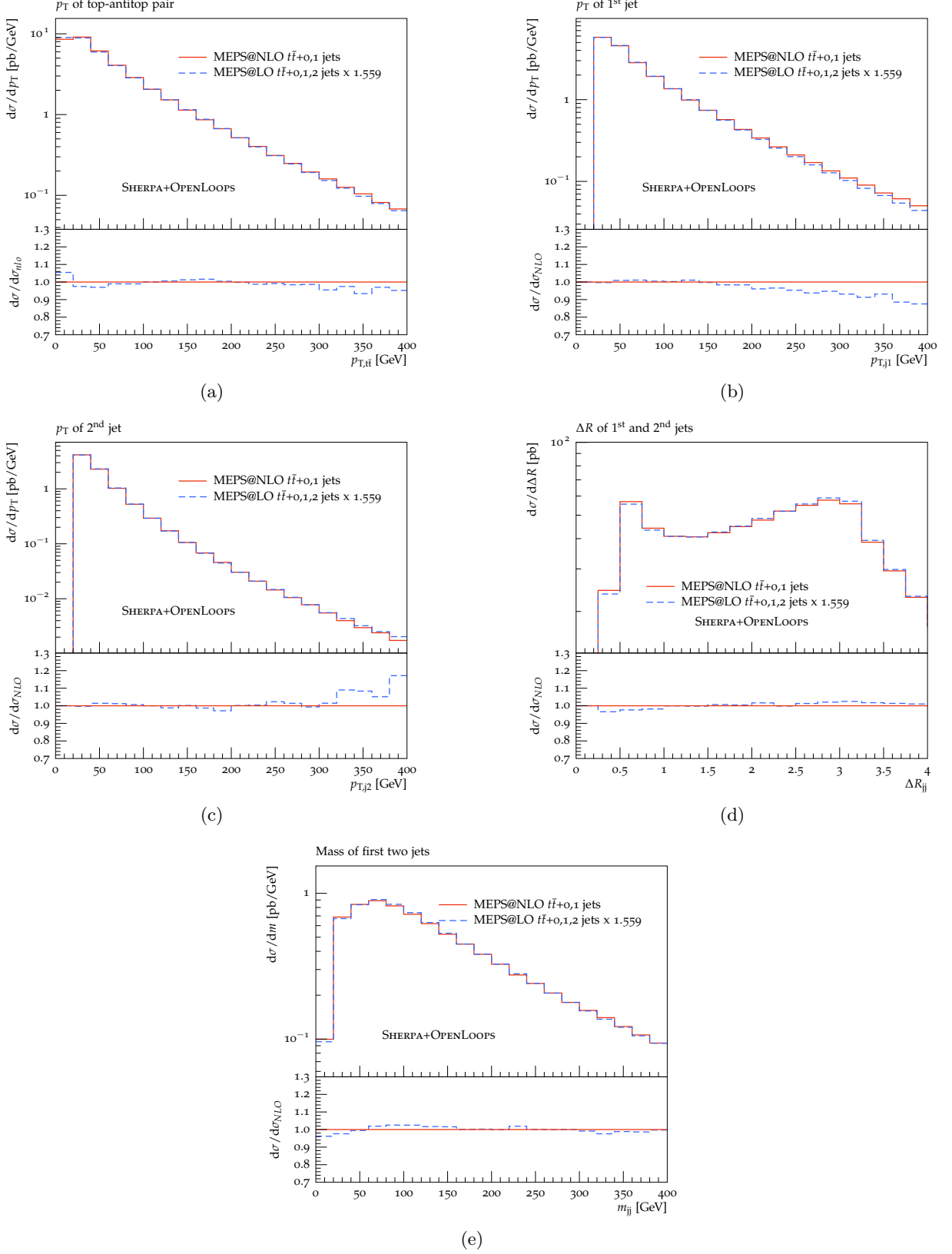


FIG. 2: Comparison of MEPS@LO  $t\bar{t} + 0, 1, 2$  jets and MEPS@NLO  $t\bar{t} + 0, 1$  jets predictions for  $p_T$  of  $t\bar{t}$  pair (2a),  $p_T$  of first (2b) and second (2c) jet,  $\Delta R$  of first two jets (2d) and invariant mass of first two jets (2e). In this comparison generic (light or heavy-flavour) jets are considered, but  $c$ - and  $b$ -jets yield only minor contributions. Top decays, hadronisation and underlying event are switched off. A constant  $K$ -factor of 1.559 is applied to the MEPS@LO simulation.

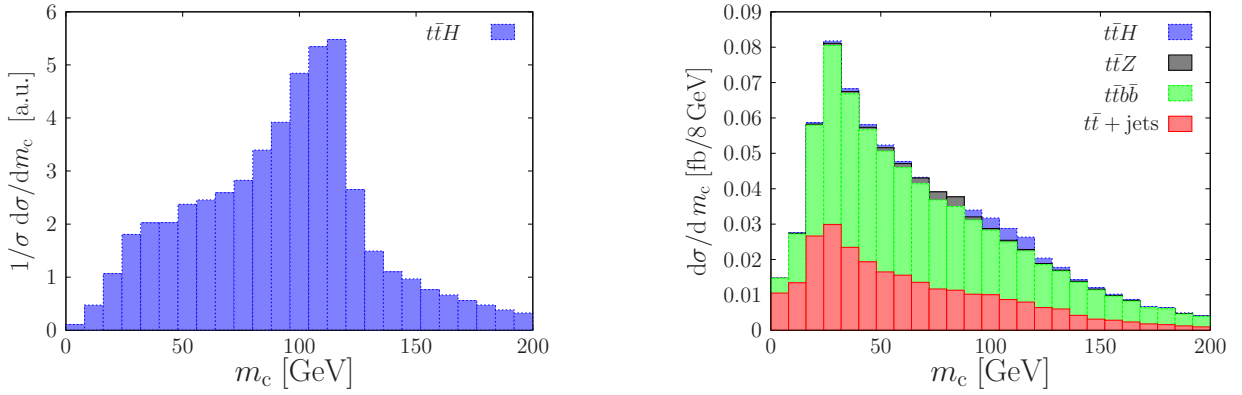


FIG. 3: Distributions in the Higgs-candidate mass,  $m_c$ , for signal (left) and signal plus  $t\bar{t} + X$  backgrounds (right) after step 6 (third  $b$ -tag) of the standard boosted analysis of Sec. III.

into Cambridge/Aachen (C/A) [66]  $R = 1.5$  fat jets with  $p_{Tj} > 200$  GeV, excluding events with less than two such fat jets. The fat jets are handled as hadronic-top and Higgs candidates.

After preselection cuts the selection enters the main stage, which is based on following jet-substructure analysis:

1. Each fat jet is tagged as  $t_{\text{had}}$  (hadronic top) or non- $t_{\text{had}}$  jet using a top tagger, and we require at least one top-tag in the event. Specifically, the HEPTopTagger is used instead of the top-tagging method described in [7]. Although two hadronic top-tags in a semi-leptonic  $t\bar{t}$  event are unlikely, there is a significant probability to misidentify a Higgs boson as a top quark (see Sec. III A). Thus, more than one fat jet can be top-tagged at this stage.
2. In the interest of retaining as much signal as possible, instead of vetoing events with more than one top-tagged jet, we identify as unique top candidate the top-tagged jet that minimises  $\Delta m_{\text{tot}} \equiv |m_{t,\text{reco}} - m_t| + \min_{ij} |m_{ij} - m_W|$ . Here  $m_{t,\text{reco}}$  is the mass of the reconstructed top and  $m_{ij}$  is the invariant mass of the pair of subjets closest to the  $W$  mass.
3. A rapidity cut  $|\eta| < 2.5$  is applied to all remaining fat jets, including top-tagged jets that have not been selected as top candidates in the previous step.
4. For each fat jet (except the top candidate) we apply the mass drop filter proposed in [7]. If the fat jet has less than two subjets after mass drops it is ignored. Otherwise the pairs of 4-momenta that survive the mass drop represent possible  $H(b\bar{b})$  structures. They are ordered according to a variant of the Jade distance [67],

$$d_{ij} = p_{Ti} p_{Tj} \Delta R_{ij}^4, \quad (1)$$

and only the first three such pairs in descending distance  $d_{ij}$  are retained. Next, the constituents of each subset pair are filtered into C/A jets of radius  $R_{\text{filt}} = \min(0.3, \Delta R_{ij})$  and  $p_T > 20$  GeV. Only the first 3 filtered jets are kept and combined into what we refer to as a *Higgs candidate*.

5. We require exactly two  $b$ -tags from the filtered subjets of the Higgs candidate.
6. We request exactly one additional  $b$ -tag in the event. This condition is applied after removing the reconstructed Higgs and top, which are supposed to involve three of the four  $b$ -quarks of a signal event, and after clustering the remaining final state objects of the Higgs fat jet into C/A jets with  $R = R_{\text{filt}}$  and  $p_T > 20$  GeV (*inner jets*), and the objects outside the Higgs fat jet into C/A jets with  $R = 0.4$  and  $p_T > 30$  GeV (*outer jets*). As the Higgs fat jet was already processed by a mass drop/grooming procedure, we choose a more aggressive jet definition.
7. We identify a Higgs candidate as tagged if its invariant mass  $m_c$  lies in the  $[100, 130]$  GeV mass window.

A first picture of the quality of the Higgs reconstruction in the boosted analysis described above is provided in Fig. 3, which displays the invariant-mass distribution of the Higgs candidate after step 6. The normalised  $m_c$  distribution for the  $t\bar{t}H$  signal (left plot) features a sharp cut-off at large  $m_c$  and a rather long low-mass tail. There we observe a bulky structure that points to Higgs misidentification, i.e. Higgs candidates that involve  $b$ -quarks from top decays. Moreover, the Higgs peak lies about 15 GeV below the true Higgs mass of 125 GeV, mainly due to uncorrected

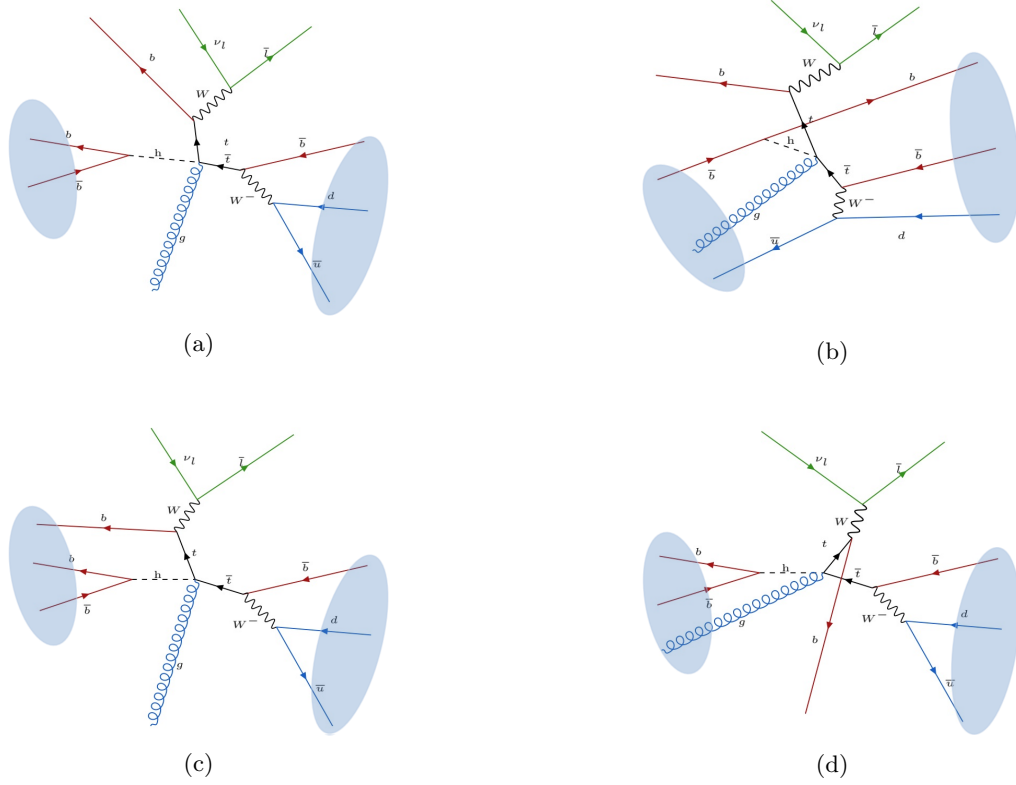


FIG. 4: Schematic representation of typical  $t\bar{t}H$  event topologies. The ellipses indicate how partons are clustered to form two fat jets. Topology 4a is the cleanest one: the Higgs products and the hadronic top products form two separate fat jets without pollution from other hard particles. Topology 4b features misassignments of the Higgs and hadronic top products. In topology 4c the hadronic top decay products form a fat jet, and the Higgs decay products form another fat jet with the leptonic top  $b$ -quark falling within it. In topology 4d the  $b$ -quark from the leptonic top decay does not pollute the Higgs fat jet, but there is a gluon radiation strong enough to form a substructure within the Higgs fat jet.

energy losses via neutrinos in  $B$ -meson decays. Superimposing the  $t\bar{t}H(b\bar{b})$  signal and the dominant  $t\bar{t} + \text{jets}$  and  $t\bar{t}b\bar{b}$  backgrounds (right plot) illustrates how the latter are dominated by the low mass region. Nevertheless, also due to a certain dilution of the  $H \rightarrow b\bar{b}$  peak, the background contamination of the signal region remains quite serious. In particular, as discussed in detail in Sec. VI, when comparing to the analysis in [7] we find a sizeable reduction of  $S/B$  in the signal region, which can be attributed to the changes in the Monte Carlo simulations of signal and background processes and to the  $b$ -jet mistagging in  $t\bar{t} + \text{jet}$  events. As a consequence, the systematic (theoretical and experimental) uncertainty on the background rate and shape may be as large or even larger than the signal. Hence for an optimal signal strength measurement in  $t\bar{t}H(b\bar{b})$  a further reduction of the background level through improved selection strategies, as well as a reduction of the related uncertainties, are of crucial importance.

As a preliminary step towards the improved  $t\bar{t}H(b\bar{b})$  selection strategies proposed in Section IV, in the following we present a detailed study of the quality of top and Higgs reconstruction in the standard boosted analysis. Specifically, we attempt to identify the patterns that dominate the reconstruction, i.e. the most probable ways how  $t\bar{t}H(b\bar{b})$  decay products are grouped into two fat jets. Such configurations will be referred to as event topologies, and some typical examples are illustrated in Figure 4. The boosted selection is targeted at the topology in Fig. 4a, where the three quarks from the  $t_{\text{had}}$  decay and the  $b\bar{b}$  pair from the Higgs decay form two separate fat jets, which do not overlap with the extra  $b$ -jet from the decay of the leptonic top,  $t_{\text{lep}}$ . However, given the number of final state objects and the size of the fat jets, the probability is large that the quarks group up in a different way to form two fat jets with  $p_T > 200$  GeV. In particular, we are interested in topologies that contribute the most to Higgs candidate misidentification, resulting in signal dilution and  $t\bar{t}H$  sensitivity losses. In the following subsection we categorise the signal events according to their quality of Higgs and top reconstruction.



label	bin	before top tag	after top tag	tagging efficiency
$A_1$	11000111	0.12	0.32	0.40
$A_2$	11001111	0.03	0.08	0.42
$A_3$	10111000	0.06	0.07	0.18
$A_4$	11010111	0.02	0.06	0.40
$A_5$	11100111	0.02	0.04	0.41
$A_6$	11011111	0.01	0.04	0.39

TABLE III: The normalised distributions of fat jets before top tagging (column 2) and top-tagged fat jet (column 3) in the dominant bins of the 8-dimensional jet-category histogram. The top-tagging efficiency (column 4) is defined as the probability that a fat jet is top-tagged in step 2 of the boosted selection. The rows are ordered by decreasing fraction after the top-tag. The bin is identified by specifying the conditions that are true (1) and false (0) in the order listed in the text. The left-most digit corresponds to the first condition.

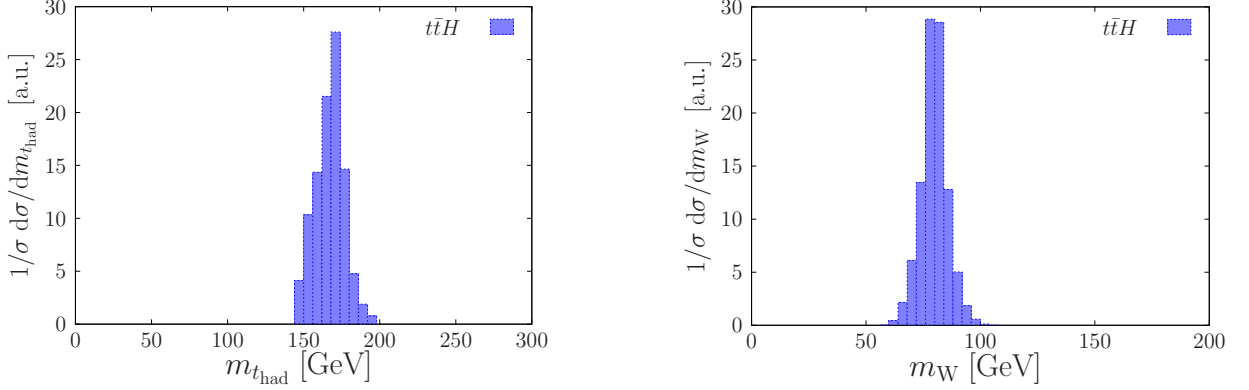


FIG. 5: Distributions of the  $m_{t_{\text{had}}}$  (left) and  $m_W$  (right) invariant masses for the cleanest topology  $A_1$  of Table III, after step 2 of the boosted analysis of Sec. III.

### A. Quality of hadronic top reconstruction

To define categories that reflect the goodness of fat jets as hadronic top candidates the following 8 binary conditions (true/false) are used:

1.  $t_{\text{had}}$ : the hadronic top quark is boosted ( $p_{T,t_{\text{had}}} > 150 \text{ GeV}$ )
2.  $t_{\text{had}}$ : the hadronic top quark overlaps with the jet ( $\Delta R_{\text{jet},t_{\text{had}}} < R_{\text{fat}}$ )
3.  $t_{\text{lep}} \rightarrow b\bar{\ell}\nu$ : the  $b$ -quark from  $t_{\text{lep}}$  belongs to the jet
4.  $H \rightarrow b\bar{b}$ : the harder  $b$  from the Higgs belongs to the jet
5.  $H \rightarrow b\bar{b}$ : the softer  $b$  from the Higgs belongs to the jet
6.  $t_{\text{had}} \rightarrow bjj$ : the  $b$ -quark from  $t_{\text{had}}$  belongs to the jet
7.  $t_{\text{had}} \rightarrow bjj$ : the harder light quark from  $t_{\text{had}}$  belongs to the jet
8.  $t_{\text{had}} \rightarrow bjj$ : the softer light quark from  $t_{\text{had}}$  belongs to the jet

This characterisation is applied to the ensemble of fat jets in the  $t\bar{t}H$  signal sample at two levels of the boosted selection: considering all fat jets just before top tagging and, alternatively, only for the jet that has been successfully top-tagged and selected as top candidate in step 2. In practice a  $t\bar{t}H$  event corresponds to at least two fat jets before top tagging and exactly one top-tagged fat jet. Each one of these fat jets falls into one bin of the 8-dimensional discrete space defined by the above conditions. Overall this amounts to 256 fat-jet categories, which will be referred to also as jet topologies in the following. It turns out that more than 60% of the top-tagged fat jets correspond to one of the six jet topologies presented in Table III.

The  $A_1$  topology corresponds to the optimal configuration, where all  $t_{\text{had}}$  decay products make up one fat jet, while the Higgs products and the  $t_{\text{lep}}$   $b$ -quark end up in another direction. As illustrated in Fig. 5, this topology features

label	bin	before $b$ -tags	after $b$ -tags	after $m_c$ cut	tag efficiency
$B_1$	110021	0.05	0.08	0.17	0.77
$B_2$	110023	0.10	0.16	0.24	0.53
$B_3$	110123	0.09	0.40	0.38	0.32
$B_4$	111023	0.01	0.03	0.03	0.31

TABLE IV: The fraction of the signal cross section at different steps of the analysis in four of the 144 bins in the 6-dimensional Higgs-jet category histogram. The tag efficiency of the topology is reported in the last column, and the bins are ordered by decreasing tag efficiency. Each row corresponds to a bin identified by specifying the conditions that are true and false (or a numerical value if applicable) in the order listed in the text. The left-most digit corresponds to the first condition.

an excellent top- and W-mass reconstruction. However, it corresponds to only one third of all events with a top-tag. For the  $A_5$  topology, where the  $b$ -quark from  $t_{\text{lep}}$  enters the fat jet of the hadronic top, we find a tagging efficiency of roughly 40%, similarly as for  $A_1$ . In fact, the top tagger is built in such a way that a top is recovered with the same efficiency irrespectively of the presence of additional structure in the fat jet. The  $A_1$  and  $A_5$  topologies allow for a good Higgs identification, since the Higgs decay products are contained in the remaining fat jet. However they represent less than 40% of the total signal after top tagging. There are other configurations, like  $A_2$ ,  $A_4$  and  $A_6$ , where parts of the Higgs boson as well as the whole top form a fat jet, for which we find again a tagging efficiency around 40% as for a fat jet containing only the top quark.

The  $A_3$  topology, where a Higgs fat jet is mistagged as a top, represents another significant contribution. The related mistag rate is around 20%, and the corresponding events often involve a second top tag associated with the correct hadronic top. Thus events with more than one top tag should not be vetoed, and it is important to select the “best” top candidate (step 2 of our selection). Obviously topologies where the reconstructed top contains one or more quarks from the Higgs decay ( $A_2$ ,  $A_4$ ,  $A_5$ ,  $A_6$ ) do not allow for a correct Higgs tag. Such configurations amounts to 55% of the signal after the top-tag stage. However, this problem is alleviated by the request of two  $b$ -tags within the Higgs candidate fat jet: if one of the Higgs  $b$ -quarks fall within the top tagged jet, then the Higgs jet will be unlikely to contain two  $b$ -quarks, and such events will be strongly suppressed in the final selection.

## B. Quality of Higgs reconstruction

To assess the the goodness of fat jets as Higgs candidates we employ categories based on the following criteria:

1.  $H$ : the Higgs boson is boosted ( $p_{T,H} > 150 \text{ GeV}$ )
2.  $H$ : the Higgs boson overlaps with the jet ( $\Delta R_{\text{jet},H} < R_{\text{fat}}$ )
3.  $t_{\text{had}} \rightarrow bj\bar{j}$ : the  $b$  quark from  $t_{\text{had}}$  belongs to the jet
4.  $t_{\text{lep}} \rightarrow b\ell\nu$ : the  $b$  quark from  $t_{\text{lep}}$  belongs to the jet
5.  $H \rightarrow b\bar{b}$ : the number of  $b$ -quarks from the Higgs decay the jet contains is 0/1/2
6.  $H \rightarrow b\bar{b}$ : the number of  $b\bar{b}$  Higgs candidates in the fat jet is 0/1/3

Note that fat jets containing at most one, two, or three  $b$ -quarks, can yield zero, one or three  $H(b\bar{b})$  candidates, respectively. Conditions number 5 and 6 have three possible outcomes. This makes a total of 144 categories, but again only few of them yield significant contributions to the accepted cross section. The relative weight of the four most important topologies is reported in Table IV at three levels of the analysis of Sec. III: before and after  $b$ -tagging (before step 5 and after 6), and after the  $m_c$  mass cut (step 7). These four leading topologies, ordered according to their relative weight after the  $m_c$  cut, account for 80% of the  $t\bar{t}H$  signal within the  $m_c$  mass window. The corresponding distributions in the invariant mass of the Higgs candidate are displayed in Figure 6. We see that, whenever the Higgs fat jet contains both Higgs  $b$ -quarks and no other partons ( $B_1$  topology), the  $m_c$  distribution features a clear peak. Of course the missing neutrinos from the  $B$ -meson decays skew and shift the peak. If, however, QCD radiation produces a third hard structure ( $B_2$  topology), the peak is smeared out due to additional continuum contributions from false Higgs candidates. This continuum contribution is greatly diminished by the double  $b$ -tag requirement for the Higgs candidate’s subjects.

The  $B_3$  topology, where the  $H \rightarrow b\bar{b}$  products in the fat jet are contaminated by a third  $b$ -quark from the leptonic top, is the main contributor after step 6 of the analysis. Since all subjects used to reconstruct the Higgs candidates are

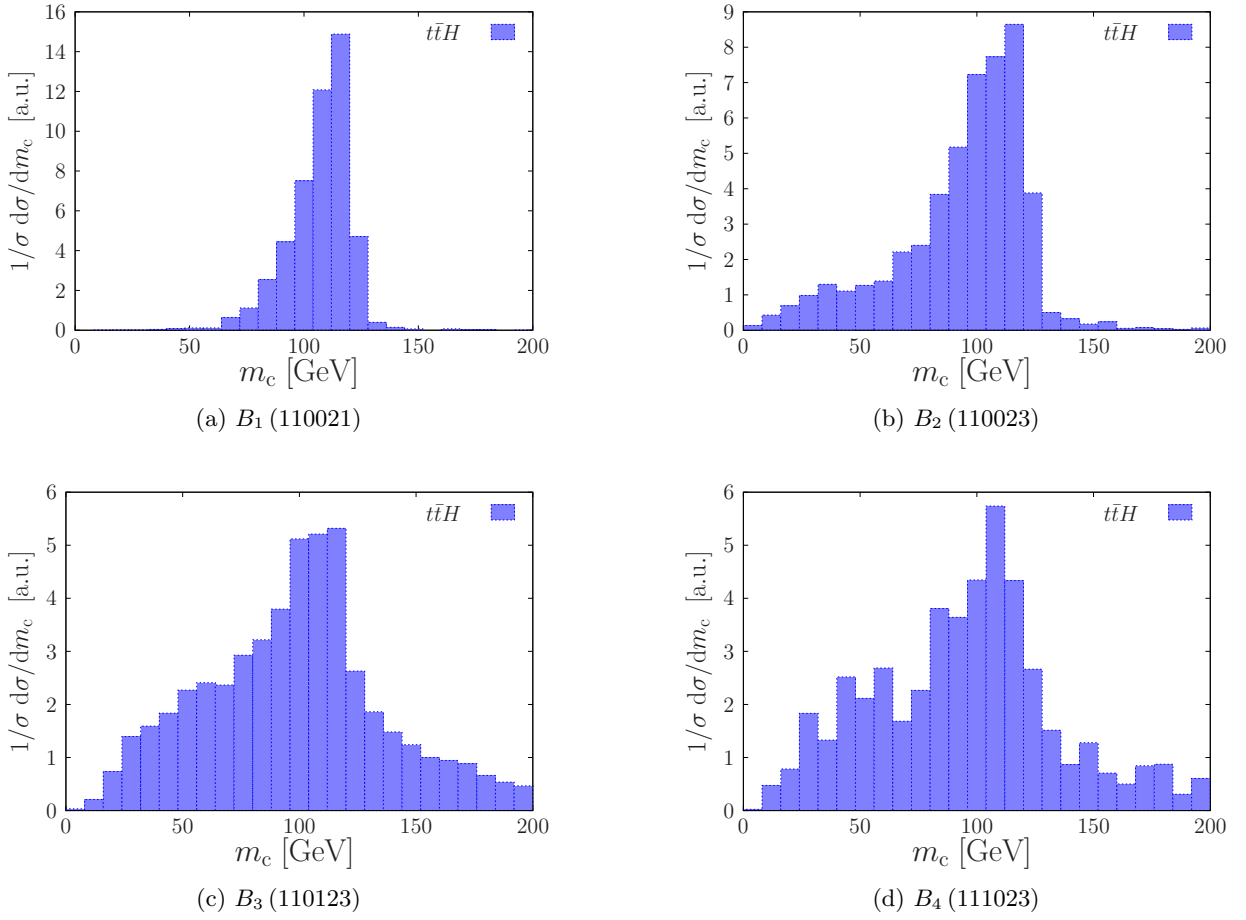


FIG. 6: Distributions of the Higgs candidate mass,  $m_c$ , for different Higgs-jet topologies after requesting three  $b$ -tags, i.e. after step 6 of the boosted analysis. The figures correspond to the topologies shown in Table IV.

$b$ -jets, the continuum distribution from a false Higgs candidate is comparable to the true peak-shaped distribution in the mass range of interest. Moreover, the continuum distribution has a similar shape as the irreducible  $t\bar{t}b\bar{b}$  background. Therefore, as discussed in the next section, in order to trim this addition to the background from falsely tagged signal and to sharpen the peak structure in presence of three-candidate fat jets, we will optimise the Higgs tag by attempting a reconstruction of the leptonic top.

#### IV. IMPROVEMENTS AND NEW AVENUES

In this section we propose new selection strategies targeted at a better reconstruction of topologies that are the major contributors to misidentified Higgs- or top-candidate fat jets. In Sec. IV A we present improvements of the standard boosted analysis of Sec. III as well as new boosted analyses that exploit phase space regions with a single fat jet. Such boosted selection strategies will be compared to a more inclusive multi-variate analysis presented in Sec. IV B.

##### A. Boosted final state configurations

The standard boosted analysis of Sec. III is targeted at Higgs candidates with topology  $B_1$ , which provides optimal Higgs reconstruction and low mistag rates (see Tab. IV and Fig. 6a). The intrinsic difficulty of any reconstruction approach is to maximise the selection efficiency for this particular topology and to optimise Higgs reconstruction in fat jet topologies that feature a less trivial substructure. To this end, it is useful to perform independent analyses depending on the number of possible Higgs candidates inside Higgs fat jets. If the fat jet contains only two hard

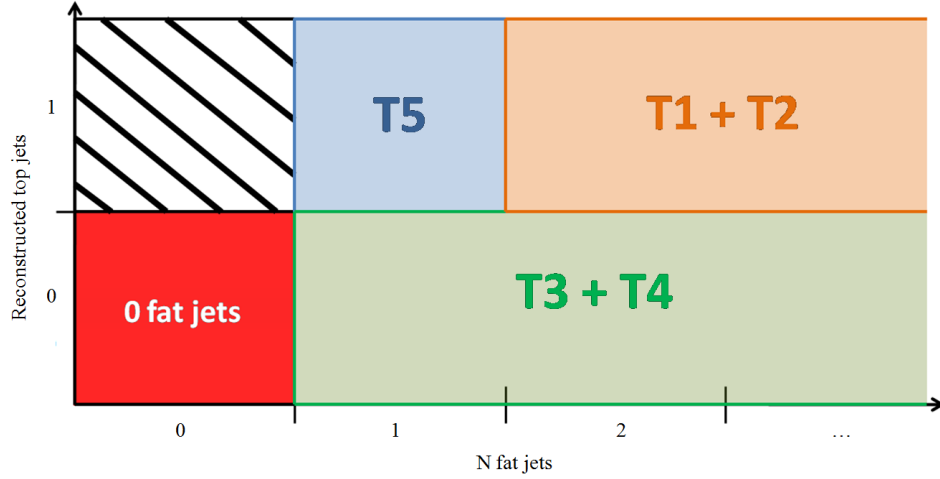


FIG. 7: The single-isolated-lepton event phase space with the explored regions labelled as in the text.

substructure objects it can only form one Higgs candidate. In this case, even though there are ways to fake the Higgs candidate (by forming a fat jet from one Higgs decay product and the leptonic top  $b$ -quark for example), our results indicate that the final selection is dominated by the desired topology, i.e. by a correctly tagged Higgs boson. In the following, we will propose improved selection strategies for the more challenging configurations with additional hard substructure objects. Furthermore, in order to increase the statistical sensitivity to the  $t\bar{t}H$  signal, we will complement the standard boosted analysis with extra channels without tagged hadronic tops or without boosted Higgs candidates. Thus we will slice the phase space of single-lepton  $t\bar{t}H$  events into the categories illustrated in Fig. 7:

**T1:**  $\geq 2$  fat jets, 1 tagged boosted top, 1 Higgs candidate

**T2:**  $\geq 2$  fat jets, 1 tagged boosted top, 3 Higgs candidates

**T3:**  $\geq 1$  fat jets, no tagged boosted tops, 1 Higgs candidate

**T4:**  $\geq 1$  fat jets, no tagged boosted tops, 3 Higgs candidates

**T5:** exactly 1 fat jet, 1 tagged boosted top, unboosted Higgs candidate

Configurations **T1** and **T2**, which will be handled separately here, cover the entire phase space of the standard boosted analysis of Sec. III. In categories **T3** and **T4** we look for a boosted Higgs and an unboosted hadronic top, and in **T5** we anticipate an unboosted Higgs after reconstructing the boosted top. All in all we examine five statistically independent phase space regions that, when combined, can enhance the sensitivity to  $t\bar{t}H$  events. Note that here we will not study events without fat jets.

### 1. Topologies **T1** and **T2**: Boosted $t_{\text{had}}$ and boosted $H$

In the following we describe dedicated selections for event categories with one (**T1**) and more (**T2**) Higgs candidates after step 4 of the standard boosted analysis of Sec. III.

As the Higgs mass peak in the **T1** channel is already fairly narrow, one way to further separate signal from  $t\bar{t} + X$  backgrounds is to exploit the colour singlet nature of the Higgs boson. The colour dipole, formed by the  $b\bar{b}$  pair, disfavours radiation away from the Higgs decay products, while  $b\bar{b}$  pairs originating from the QCD background feature a different radiation pattern. In order to take advantage of this distinctive signal feature we use the ellipticity jet-shape variable  $\hat{t}$  [68] computed in terms of the Higgs candidate's constituents. Figure 8 shows the different mass distributions of the Higgs candidate in the **T1** selection channel with and without a cut  $\hat{t} < 0.2$ . As discussed in Sec. VI, the ellipticity cut allows one to achieve an appreciable improvement in  $S/B$  with minor losses in terms of signal yield. However, given its fairly small cross section, the **T1** channel alone does not provide substantial sensitivity to  $t\bar{t}H$  at Run 2.

The complementary category **T2** has a four times higher rate. Thus, increasing  $S/B$  in this channel, which is dominated by the Higgs-jet topology B3 in Tab. IV, can boost the sensitivity of  $t\bar{t}H(b\bar{b})$ . To this end, after step 4 of

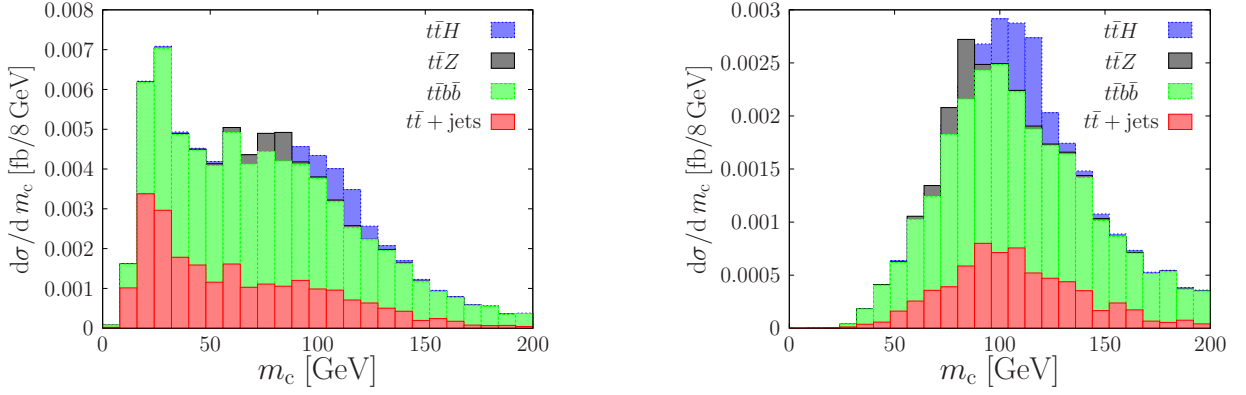


FIG. 8:  $m_c$  distribution from the selection channel with a single Higgs candidate in the fat jet and a tagged boosted hadronic top (**T1**). The left(right) figure is without(with) a  $t$  cut on the Higgs candidate constituents.

the standard boosted analysis, we try to tag the leptonic top,  $t_{\text{lep}}$ , as well as the Higgs if the fat jet has more than one Higgs candidate. The reconstruction of  $t_{\text{lep}}$  helps to uniquely identify the origin of the three  $b$ -tagged jets and ameliorates the combinatorial smearing of the Higgs peak evident in Fig. 6c. The reconstruction is implemented by minimising a  $\chi^2$  score computed for all combinations of final state objects that can form a Higgs- $t_{\text{lep}}$  pair. For each of the three Higgs candidates there are a number of possible combinations, and the relevant physical objects are:

1. two subjects reconstructed from the hadrons of the filtered Higgs candidate using the exclusive- $k_T$  algorithm.
2. the inner and outer jets with respect to the current Higgs candidate (see definition in Sec.III);
3. the isolated lepton;
4. the missing transverse momentum of the event  $\cancel{E}_T$ .

The neutrino momentum can be reconstructed from the lepton momentum and  $\cancel{E}_T$  imposing the on-shell condition for the corresponding  $W$  boson. The ambiguity related to the two solutions of the quadratic equation is not resolved at this point, i.e. both possibilities are taken into account in the following steps. Since a leptonic top consists of a  $b$ -quark, a charged lepton and a neutrino, we call a  $Ht_{\text{lep}}$  configuration any unique choice of one out of  $n$  inner and outer jets, one of the two neutrino candidates, the isolated lepton and the two exclusive Higgs candidate subjets. Therefore, any 3-Higgs-candidate fat jet has a number  $2 \sum_{i=1}^3 n_i$  of  $Ht_{\text{lep}}$  configurations. We define  $\chi^2$  for a configuration in the following way:

$$\begin{aligned} \chi^2 &= \chi_{\text{top}}^2 + \chi_{\text{Higgs}}^2, \\ \chi_{\text{top}}^2 &= \frac{(m_{t_{\text{lep}}, \text{reco}} - m_{t_{\text{had}}, \text{max}})^2}{\sigma_{t_{\text{had}}}^2}, \\ \chi_{\text{Higgs}}^2 &= \frac{(m_{H, \text{reco}} - m_{H, \text{max}})^2}{\sigma_{H+}^2} \Theta(m_{H, \text{reco}} - m_{H, \text{max}}) + \frac{(m_{H, \text{reco}} - m_{H, \text{max}})^2}{\sigma_{H-}^2} \Theta(m_{H, \text{max}} - m_{H, \text{reco}}), \end{aligned} \quad (2)$$

where  $\Theta$  is the Heaviside step function. The errors  $\sigma_{H\pm}$  are the standard deviations of Gaussian fits to the data to the right (+) and left (-) of the peak in **T1** (Fig. 6a). We make this choice because the reconstructed Higgs mass distribution is heavily skewed to lower values, thus a single Gaussian fit will overestimate one and underestimate the other deviation. We take  $m_{H, \text{max}}$  as the position of the peak. The  $t_{\text{had}}$  mass distribution from the topology  $A_1$  in Table III is much more symmetric. Therefore, a single Gaussian fit suffices to extract  $\sigma_{t_{\text{had}}}$  and  $m_{t_{\text{had}}, \text{max}}$ . We order all configurations in ascending  $\chi^2$  and choose the first quarter of unique configurations. Then we keep the configurations with two successful  $b$ -tags in the Higgs candidate and another for the inner or outer jet (there is only one such object per configuration). We record the Higgs candidate mass  $m_c$  of each of the configurations remaining after the  $\chi^2$  and  $b$ -tag cuts.

The  $\chi^2$  ordering complements the  $b$ -tagging in the following way. Assume the Higgs fat jet contains both the  $b$ -quark of  $t_{\text{lep}}$  and the two Higgs decay products. Without ranking the different configurations, all three Higgs candidates will certainly contribute to the  $m_c$  distribution. We ameliorate combinatorial issues by removing configurations with

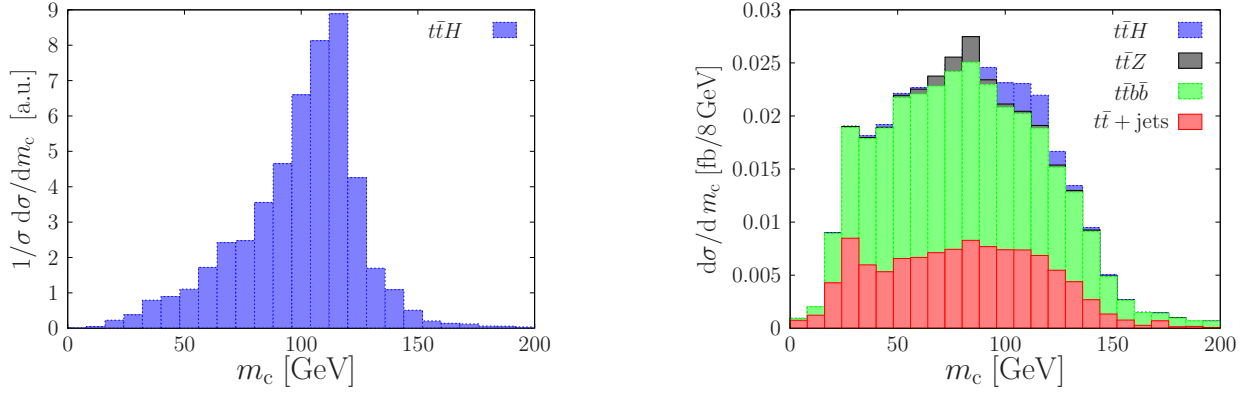


FIG. 9:  $m_c$  distribution obtained from the 25% of configurations with lowest  $\chi^2$  score in the 3-Higgs-candidate selection channel (**T2**). The left figure is the signal  $t\bar{t}H$  and the figure to the right contains signal and background.

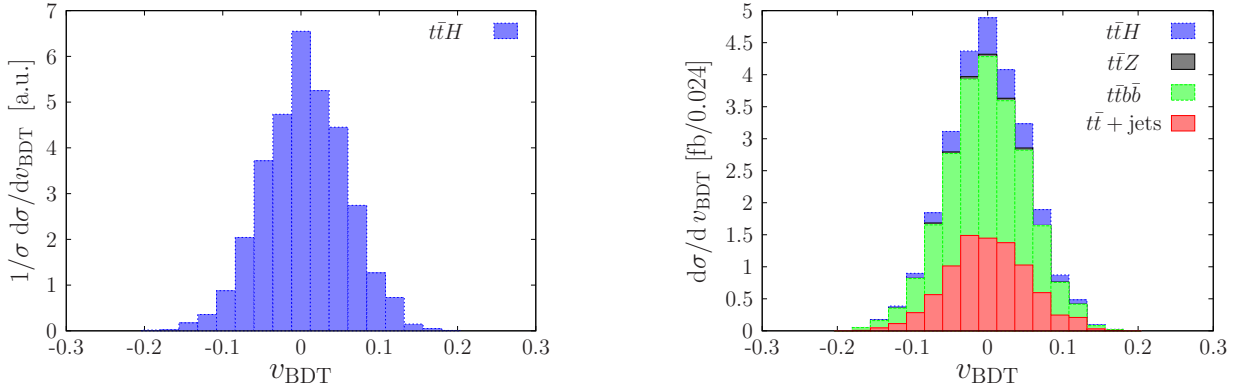


FIG. 10: Boosted Decision Trees score distribution from 5 variables calculated with the reconstructed  $t\bar{t}H$  objects after the mass cut in **T2**. The left figure is the signal  $t\bar{t}H$  and the figure to the right contains signal and background.

large  $\chi^2$  scores, i.e. we only keep the 25% of combinations with lowest  $\chi^2$  score. By requiring three  $b$ -tags, we remove the configurations that contain non- $b$ -tagged inner/outer jets. Consequently, we veto the correct configuration less often than the one where the  $b$ -quark from the leptonic top fakes one of the Higgs decays, before  $b$ -tagging of the Higgs candidate is even implemented. Figure 9 shows the change of  $m_c$  in the **T2** topology (compare with Figure 6c).

There are additional steps that one can study to remove fake configurations before applying the  $b$ -tags. We studied the impact of including the jet shape observable  $\hat{t}$  and the helicity angle [69] between the bottom quark and the charged lepton. However, we found them not to be efficient in increasing  $S/B$  at this stage of the analysis.

At this point we have reconstructed all three resonances in  $t\bar{t}H$ . Therefore, it is conceivable to use them in a multi-variate analysis (MVA) to exploit any angular dependencies between these fundamental objects. In particular we select the mass,  $p_T$  and rapidity of the  $t\bar{t}H$  system as well as the angles between the Higgs and the top/anti-top in the  $t\bar{t}H$  centre of mass frame to build a boosted decision tree (BDT) discriminant. For the numerical evaluation we use the TMVA [70] package of ROOT [71]. We build a forest of 850 trees each with three layers and require at least 5% of signal in each leaf node to explicitly avoid any overtraining. There is a great freedom of choice for the number and nature of variables in a MVA at this stage, depending on the remaining statistics and the systematic uncertainties of the input variables. Particularly the latter requires a full detector simulation for a reliable estimate. The distribution of the BDT score is displayed in Figure 10. Despite the previously described attempts at improving the  $S/B$  of **T2**, the results presented in Sec. VI indicate that the obtained improvement in  $S/B$  is rather modest.

## 2. Topologies **T3–T5**: boosted $t_{\text{had}}$ or boosted **H**

So far we have only used the selection channels where a fat jet has been tagged as a top, and there is at least one more fat jet to be tagged as a Higgs (**T1** and **T2**). In the following we will consider two additional types of channels.

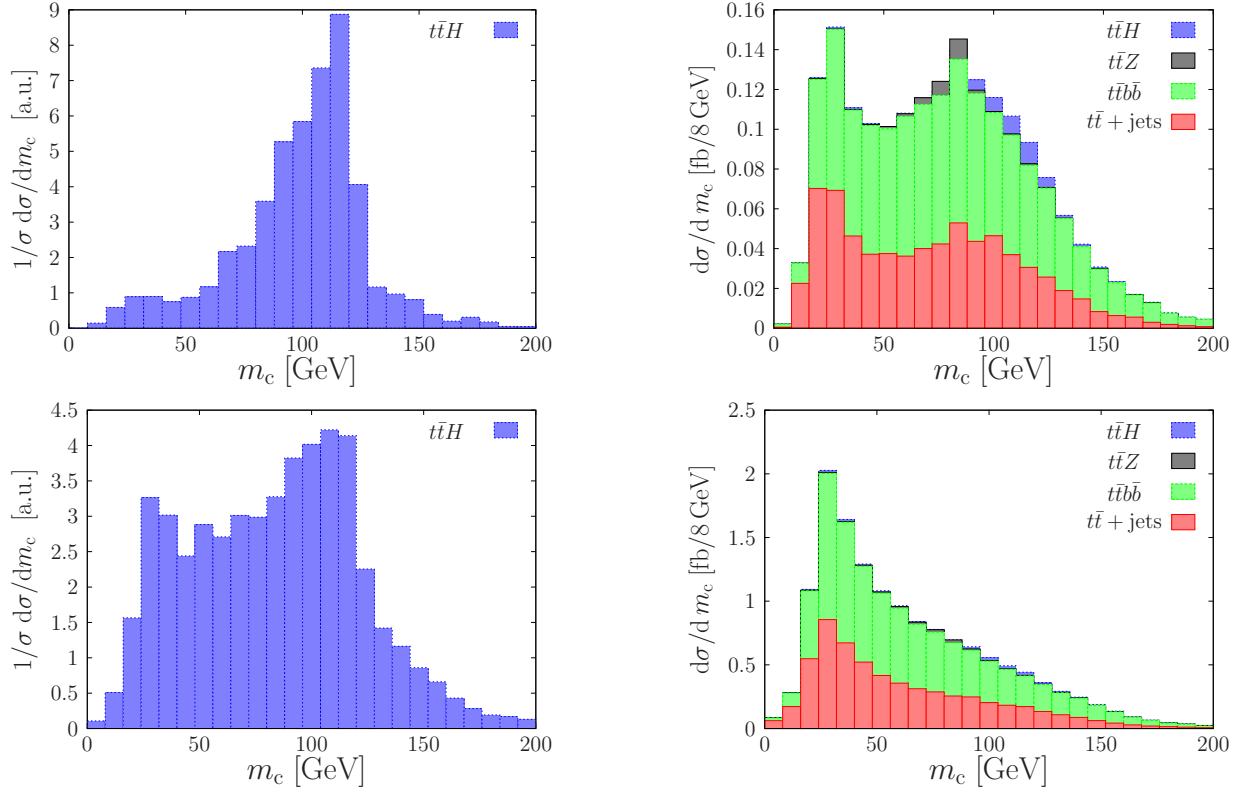


FIG. 11:  $m_c$  distribution obtained from the selection channels without any top tags - **T3** (top) and **T4** (bottom). The left figures show the  $ttH$  signal only and the figures to the right contain signal and background.

If there is one or more fat jets in the event but neither is top-tagged, we will test for a boosted Higgs among them and aim to reconstruct a top using the radiation outside the Higgs candidate (channel **T3–T4**). Vice versa, if there is only one fat jet and it has been top-tagged, we will look for a non-boosted Higgs among the remaining particles in the event (channel **T5**). In the first case (**T3** and **T4**) we follow Sec. IV A 1 for the reconstruction of the Higgs candidate. For each fat jet we find the mass drop subjects and we group them into Higgs candidates. Then we keep fat jets with up to three candidates, but we separate the 1-candidate (**T3**) from the 3-candidate (**T4**) fat jets. We again construct inner and outer jets after removing the Higgs candidates, see step 6 of the boosted analysis in Sec. III. As we would like to reconstruct the unboosted hadronic top as well, we require at least four inner or outer jets, accounting for the hadronic decay products of the leptonically and hadronically decaying top quarks.

There is a three-fold way to assign the  $b$ -quark within the hadronic top. To remove this ambiguity, we first reconstruct the hadronic  $W$  by minimising  $\Delta m_W = |m_{W_{\text{reco}}} - m_W|$ . Eventually, a  $\chi^2$  value of every  $t_{\text{had}}$  and Higgs candidate configuration is calculated, i.e.

$$\begin{aligned}
 \chi^2 &= \chi_{\text{top}}^2 + \chi_W^2 + \chi_{\text{Higgs}}^2, \\
 \chi_{\text{top}}^2 &= \frac{(m_{t_{\text{had}}, \text{reco}} - m_{t_{\text{had}}, \text{max}})^2}{\sigma_{t_{\text{had}}}^2}, \\
 \chi_W^2 &= \frac{(m_{W_{\text{had}}, \text{reco}} - m_{W_{\text{had}}, \text{max}})^2}{\sigma_{W_{\text{had}}}^2}.
 \end{aligned} \tag{3}$$

The  $\chi_{\text{Higgs}}^2$  and  $\chi_{\text{top}}^2$  are identical to the ones defined in Sec. IV A 1. The  $\chi_W^2$  parameters are extracted in the same way as the  $\chi_{\text{top}}^2$  parameters, i.e. using a Gaussian fit to the mass distribution (right plot in Fig. 5) of the two  $W$  subjects in the reconstructed hadronic top, in the case when it falls into the cleanest topology (A1) in Table III. The configurations are ordered by  $\chi^2$  and the highest 75% are rejected. From each remaining configuration, three successful  $b$ -tags are required—two among the Higgs candidate filtered subjects and another for the leptonic top. We do not require an additional  $b$ -tag for the hadronic top candidate. As before, the Higgs candidates' masses of all surviving configurations are recorded, and the resulting distributions plotted in Figure 11. Results in Sec. VI confirm

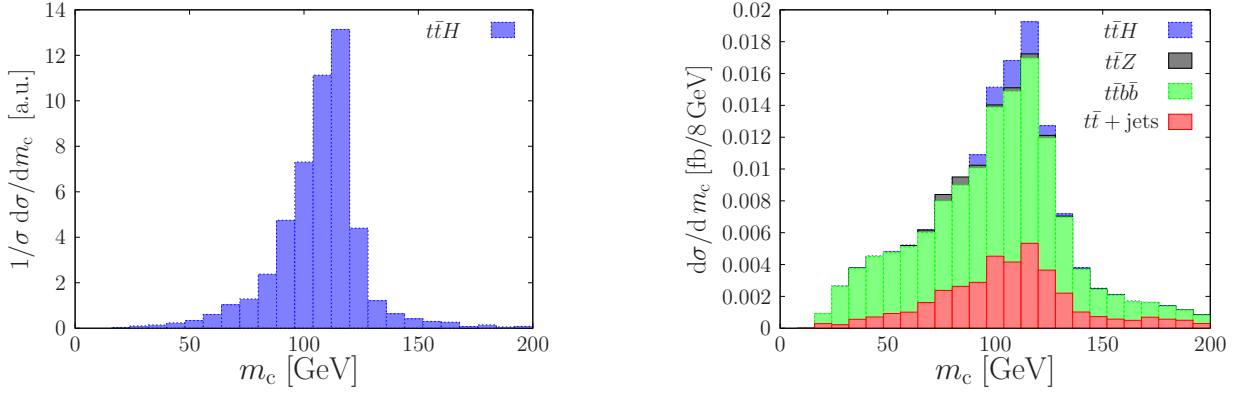


FIG. 12:  $m_c$  distribution obtained from the selection channel with only one fat jet that has been top-tagged (**T5**). The left figure is the signal  $t\bar{t}H$  and the figure to the right contains signal and background.

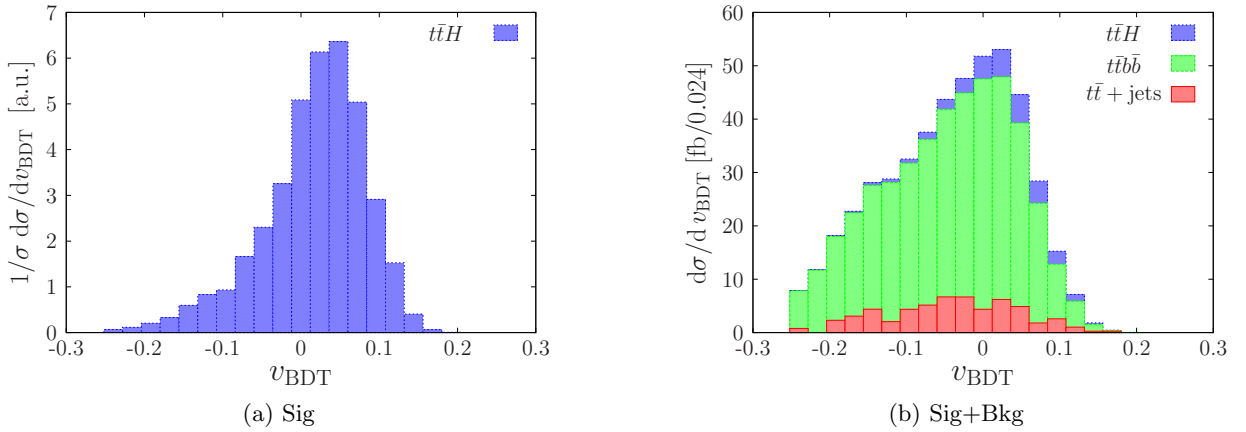


FIG. 13: Boosted Decision Trees score distribution from 7 variables calculated from objects in the non-boosted analysis. The left figure is the signal  $t\bar{t}H$  and the figure to the right contains signal and background.

that, as expected, topology **T3** features a cleaner peak and therefore a better  $S/B$  ratio than **T4**. Most importantly, the signal yields of those two channels, at approximately 1 fb, are an order of magnitude larger than for **T1** and **T2**.

Finally we focus on the channel with a single fat jet that is top tagged (**T5**). In this case we cluster all final state hadrons into C/A  $R = 0.4$  jets with  $p_T > 30$  GeV and require 3  $b$ -tagged jets. We reconstruct a Higgs and a leptonic top using the same  $\chi^2$  as in the **T2** scenario of Sec. IV A 1. The  $Ht_{\text{lep}}$  configuration consists of two  $b$ -tagged jets (Higgs candidate), the other  $b$ -jet, and a reconstructed neutrino ( $t_{\text{lep}}$ ). We calculate the  $\chi^2$  defined in Eq. 2 and choose the Higgs candidate with best  $\chi^2$  value. Figure 12 shows this candidate's mass distribution. It turns out that the **T5** channel has a  $S/B$  ratio similar to **T3**, but the signal yield is smaller by a factor of five and the background shape is more biased (see Sec VI).

## B. MVA Without Boost

As a generalisation of the boosted configurations discussed in Secs. III-IV A, we perform a MVA with seven observables that do not require any of the resonances to be boosted. The analysis may include parts of all phase space regions defined in Fig. 7, however the input objects to the observables are different. We start by asking for a single isolated lepton and at least six C/A  $R=0.4$  jets with  $p_T > 30$  GeV, of which exactly four must be  $b$ -tagged. We will only use six jets for the reconstruction, thus from the remaining jets without a  $b$ -tag we keep the two with largest  $p_T$ .



Using these six jets ( $b_1, b_2, b_3, b_4, q_1, q_2$ )<sup>¶</sup>, as well as the isolated lepton  $\ell$  and missing energy  $\cancel{E}_T$ , we define simple kinematic variables:  $\Delta m_H = \min_{ij} |m_{H,\max} - m_{b_i b_j}|$ ,  $p_{Tq_2}/p_{Tq_1}$ ,  $\max_{ij} \Delta R_{b_i b_j}$ ,  $\min_i \Delta R_{W, b_i}$ ,  $\Delta \phi_{\cancel{E}_T, b_3}$ ,  $\Delta R_{\ell, b_3}$ ,  $\Delta R_{W, b_4}$ . We found these seven variables to have highest rank, as defined in [70], after running all possible kinematic combinations of our input objects, using a BDT. Signal and background distributions in the BDT discriminant are plotted in Figure 13, and detailed results of this analysis are presented in Sec. VI.

## V. EFFECTS FROM B-JET ENERGY CORRECTION

Throughout Secs. III and IV we have neglected energy corrections of b-tagged (sub)jets. As a result, the mass of the reconstructed Higgs candidate and the top quark show a broad, smeared-out distribution. ATLAS and CMS apply jet-energy corrections to compensate for energy losses from unobserved neutrinos in the decay of  $B$ -mesons. While the correct inclusion of these corrections requires a full detector simulation and is beyond the scope of this analysis, at the end of Sect. VI we will present the most optimistic results for the  $t\bar{t}H$  reconstruction by including the neutrino momenta in the jet finding.

Distributions in the Higgs-candidate invariant mass with full  $B$ -reconstruction are illustrated in Figure 14 for all analysis channels (**T1–T5**). As compared to Figs. 8–12, including the neutrino momenta results in a narrower and more pronounced mass peak at  $m_H = 125$  GeV. This effect is especially pronounced in the **T1** channel. In this case, using an optimal mass window can increase the  $S/B$  ratio up to 40% without losing signal yield. Moreover, for the **T1** channel a side-band analysis appears to be possible where the signal strength can be estimated by comparing the  $Z$  boson peak with the adjacent Higgs peak, while the signal depleted regions can be exploited for a data driven background determination. However, the **T1** channel collects only a modest fraction of the  $t\bar{t}H$  signal (see Sect. VI), while it is evident from Fig. 14 that the other channels do not benefit in a similar way from an improved reconstruction of  $B$ -decays.

## VI. RESULTS

We present the results of the analyses described in the previous three sections in terms of  $S/B$  ratios in signal enriched regions and in the form of 95% CL limits on the signal strength  $\mu$ . We define  $\mu$  as the observed deviation from the signal plus background SM hypothesis as a fraction of the SM  $t\bar{t}H$  cross section,  $\mu = \frac{\sigma^{\text{obs}} - \sigma_{S+B}^{\text{SM}}}{\sigma_{S+B}^{\text{SM}}}$ . Therefore,  $\mu = 0$  represents no deviation from the SM<sup>||</sup>, while coupling modifications due to new physics could result in  $\mu < 0$  or  $\mu > 0$ . The limits are obtained from the final discriminating observables of the various selections, i.e. the  $m_c$  or  $v_{\text{BDT}}$  distributions. More precisely, we perform a two-sided frequentist test with the profile likelihood test statistic and the CLs variant of the p-value using the RooStats framework [72]. We use the expected number of signal plus background SM events in each bin of the relevant distribution as the null hypothesis and we look for the limits this analysis could impose on BSM contributions to the signal strength (both positive and negative). The results from the statistical analysis are presented in Fig. 15 under the assumption of a constant normalisation uncertainty of 15% for the SM background. In Fig. 16 a more optimistic scenario is presented, where the background uncertainty starts decreasing as the inverse square root of the integrated luminosity above  $300 \text{ fb}^{-1}$ . The green bands in Figs. 15–16 cover the  $\mu$  values that cannot be excluded at 95% CL assuming the data is exactly as predicted by the SM. The yellow bands extend this region to include an upward (downward) fluctuation by  $1\sigma$  of the SM median when calculating the upper (lower) 95% confidence limit.

### A. Standard boosted analysis

Let us start discussing the results of the analysis of Sec. III, which represents a standard boosted selection along the lines of [7]. The signal and background contributions at various steps of the selection are presented in Table V, and the overall picture is qualitatively similar to the original boosted analysis [7]. However the quantitative differences are quite notable. In particular, for the  $S/B$  ratio after the  $m_c$ -cut we observe a reduction from about\*\* 35% in [7] to 14%.

<sup>¶</sup>The numbering scheme signifies the  $p_T$  in descending order.

<sup>||</sup>Note that the usual  $t\bar{t}H$  signal strength corresponds to  $1 + \mu$ .

<sup>\*\*</sup>To be precise, the  $S/B$  ratios reported in [7] are 42% and 28% for  $m_H = 120$  GeV and 130 GeV, respectively.

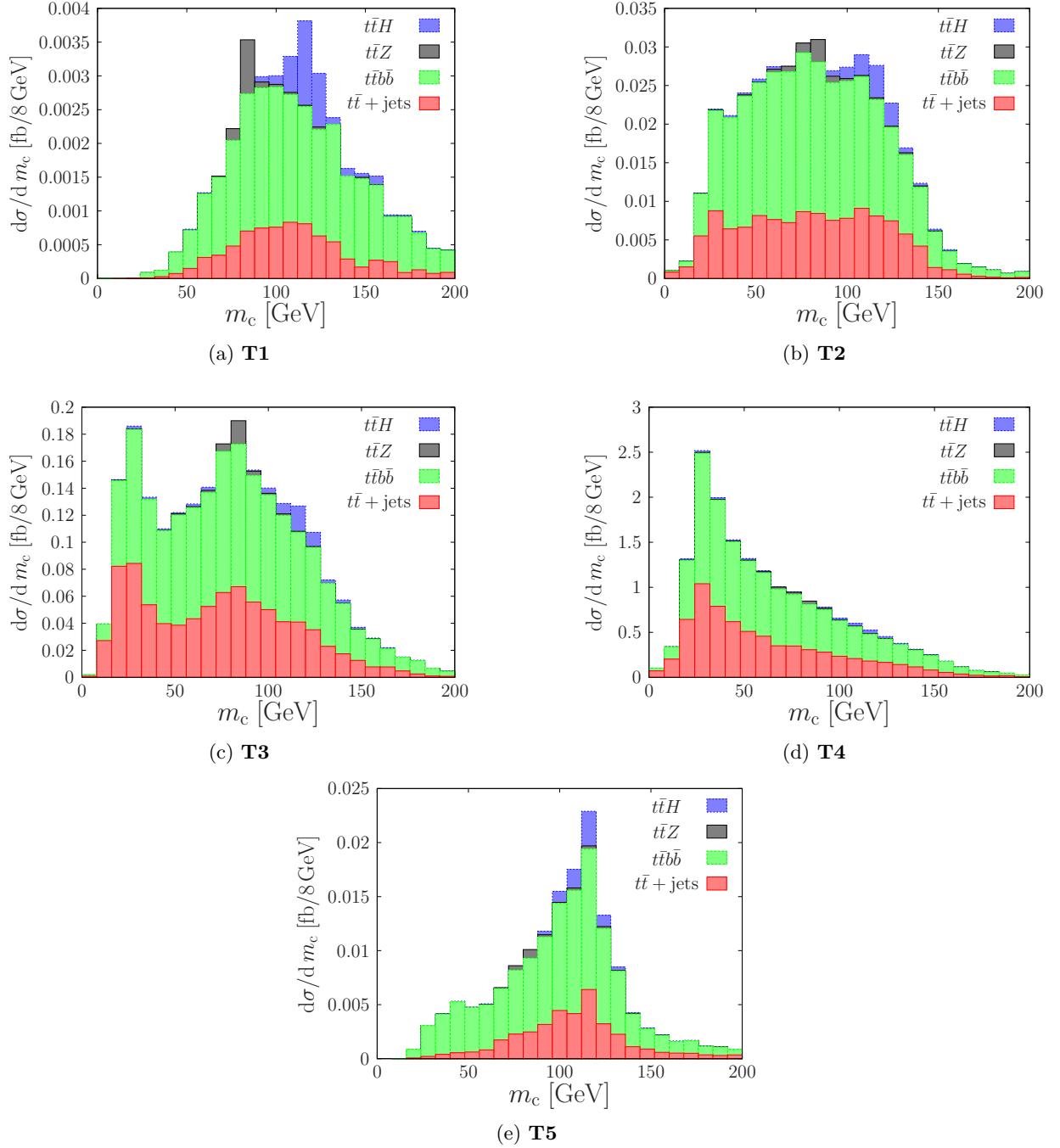
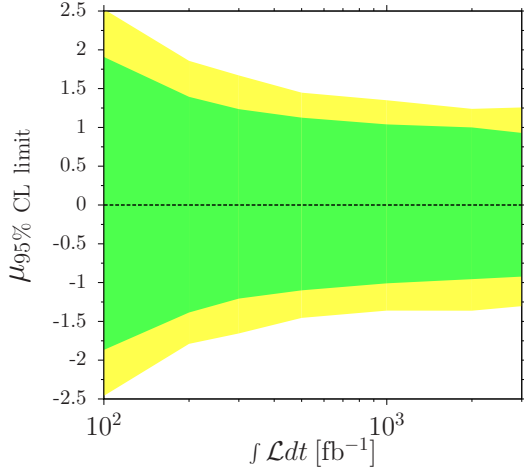


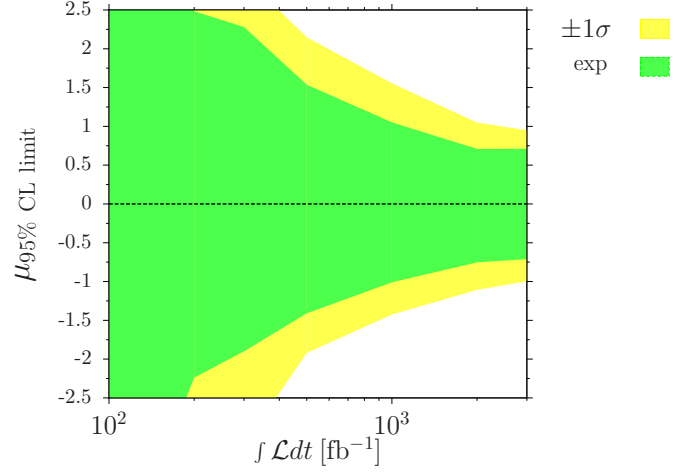
FIG. 14: Distributions in the Higgs-candidate mass  $m_c$  after three  $b$ -tags for the various selection topologies as in Figs. 8–12, but including neutrinos in the reconstructed  $B$ -hadrons.

To a very large extent, this loss of discriminating power can be attributed to the differences in signal and background rates between the two analyses. In particular, the dominant effects are a 35% increase—driven by  $t\bar{t} + \text{jets}$ —of the overall background level, and a 30% reduction of the  $t\bar{t}H$  signal within final selection cuts. As for the modified top taggers and the inclusion of  $B$ -meson decays with related neutrino-energy losses (which require a modified Higgs-mass window), we checked that the impact on  $S/B$  is relatively small.

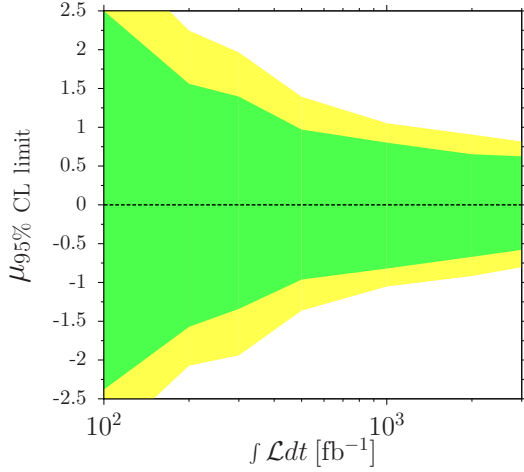
The NLO tools used in the present study (see Sect. II) provide more reliable signal and background simulations as compared to the LO+PS samples employed in [7]. In the case of the  $t\bar{t} + \text{jets}$  background we observe a very large enhancement—close to one order of magnitude in the signal region—that can be in part attributed to the usage of a rather crude approximation based on  $t\bar{t} + 1\text{jet}$  LO matrix elements matched to Herwig++ in [7]. Moreover,



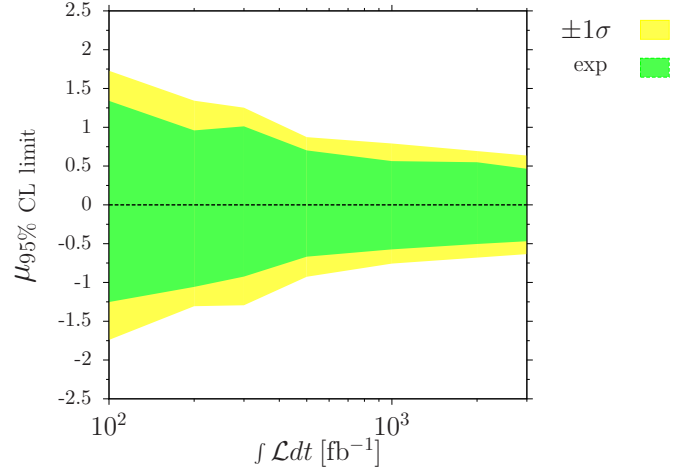
(a) Analysis of Sec. III including all relevant topologies (**T1** and **T2**).



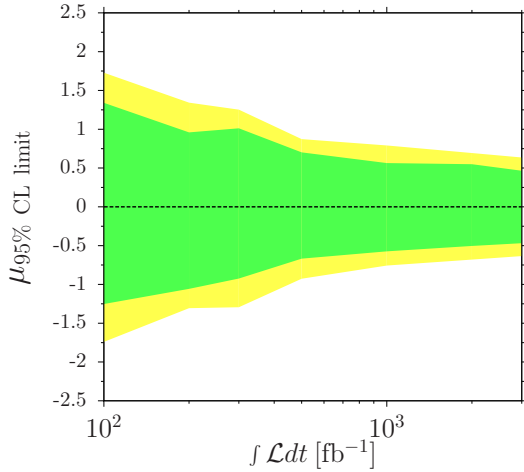
(b) Analysis of Sec. IV limited to topology **T1**.



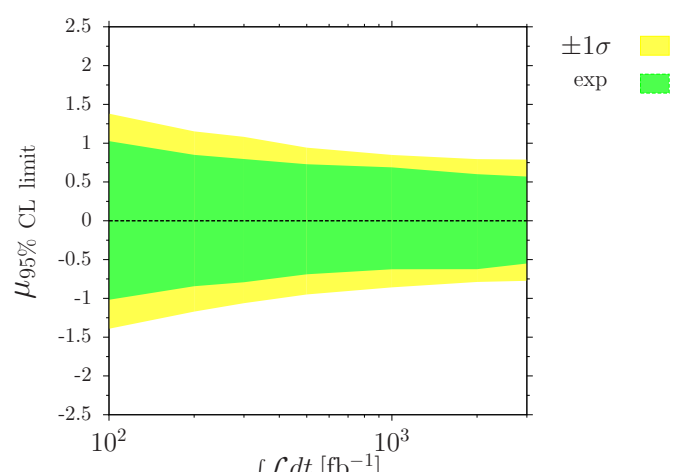
(c) Analysis of Sec. IV including topologies **T1** and **T2**.



(d) Analysis of Sec. IV including all topologies (**T1–T5**).

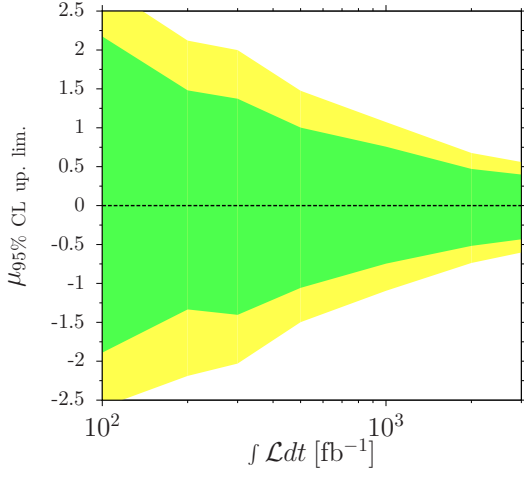
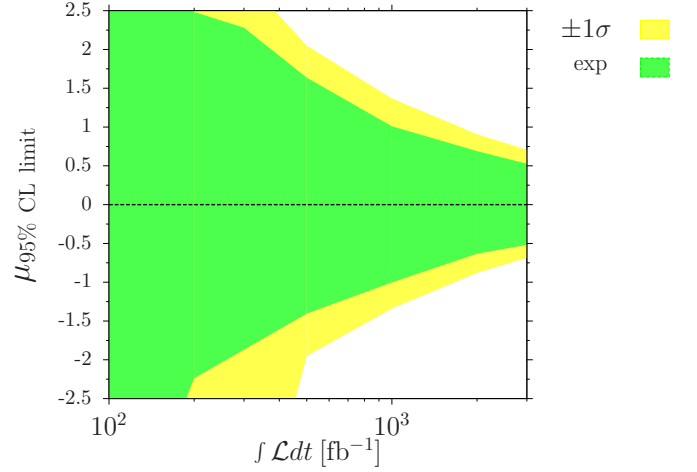
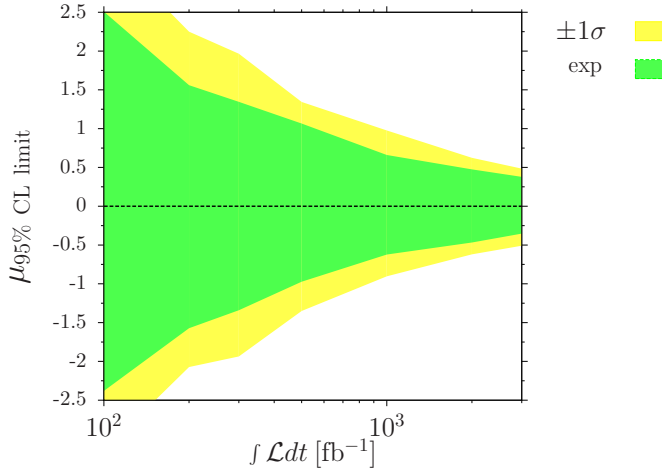
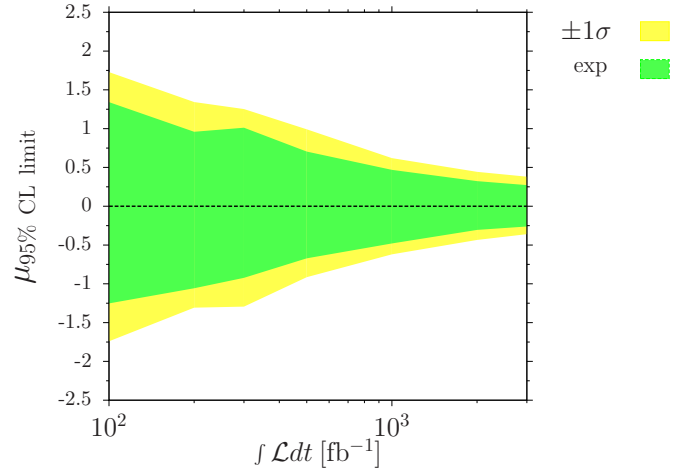
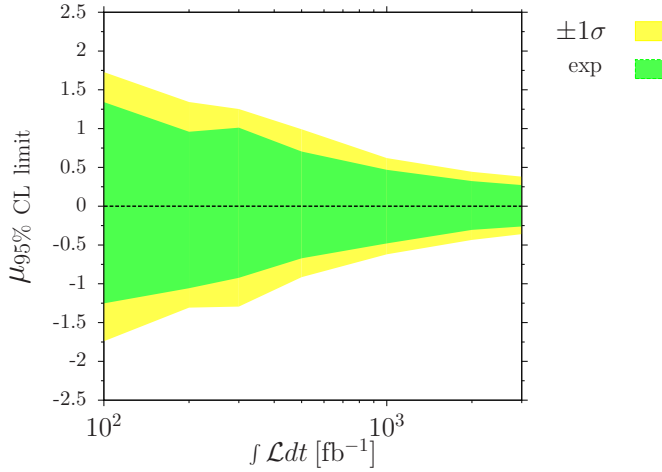
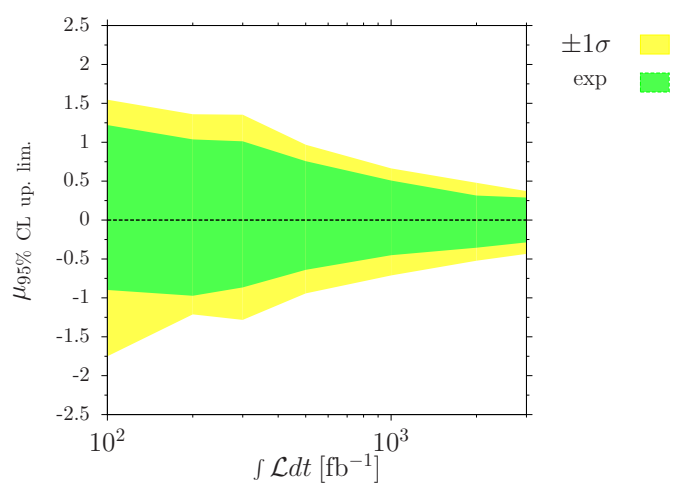


(e) Analysis of Sec. IV including all topologies (**T1–T5**) and neutrinos in  $B$ -decay reconstruction.



(f) Unboosted BDT analysis of Sec. IV B.

FIG. 15: Two-sided 95% CL limit of the signal strength  $\mu$  as a function of the integrated luminosity assuming a constant 15% normalisation uncertainty for the SM background.

(a) Analysis of Sec. III including all relevant topologies (**T1** and **T2**).(b) Analysis of Sec. IV limited to topology **T1**.(c) Analysis of Sec. IV including topologies **T1** and **T2**.(d) Analysis of Sec. IV including all topologies (**T1–T5**).(e) Analysis of Sec. IV including all topologies (**T1–T5**) and neutrinos in  $B$ -decay reconstruction.

(f) Unboosted BDT analysis of Sec. IV B.

FIG. 16: Two-sided 95% CL limit of the signal strength  $\mu$  as a function of the integrated luminosity assuming a normalisation uncertainty for the SM background that remains constant at 15% level up to  $300 \text{ fb}^{-1}$  and scales as  $1/\sqrt{\mathcal{L}}$  for higher integrated luminosities.

stage	$t\bar{t}H$	$t\bar{t}b\bar{b}$	$t\bar{t}+\text{jets}$	$t\bar{t}Z$	$S/B$
MC level	94	$7.3 \times 10^3$	$2.6 \times 10^5$	50	$3.5 \times 10^{-4}$
1 lepton	60	$4.7 \times 10^3$	$1.6 \times 10^5$	22	$3.6 \times 10^{-4}$
>1 fat jets	15	400	$9.5 \times 10^3$	5.9	$1.5 \times 10^{-3}$
1 top tag	4.8	110	$2.6 \times 10^3$	1.9	$1.8 \times 10^{-3}$
3 $b$ -tags	0.59	7.6	4.2	0.25	0.049
$m_c$ cut	0.2	0.9	0.48	0.023	0.14

TABLE V: Signal and background cross sections in femtobarn and  $S/B$  ratios at different stages of the boosted analysis of Section III.

the large relative increase of the  $t\bar{t}+\text{jets}$  contribution can be explained in part by the way we simulate  $b$ -tagging and top-tagging. On the one hand, Table V shows that imposing three  $b$ -tags results in a reduction of the signal by about a factor ten, which is well beyond the naive expectation of a suppression factor  $\epsilon_b^{-3} \simeq 3$  for a constant  $b$ -tagging efficiency  $\epsilon_b = 0.7$ . This observation can be explained by the fact that, in the present analysis, each  $b$ -tag is accompanied by a  $B$ -meson acceptance cut  $p_{T,B} > 10 \text{ GeV}$  and by the requirement that the  $B$ -meson is matched to the actual jet. In particular, this latter condition can be rather restrictive in case of the two narrow  $b$ -jets that form the Higgs candidate substructure. On the other hand, it turns out that applying three  $b$ -tags to the  $t\bar{t}+\text{jets}$  background results in a suppression factor  $2600/4.2 \simeq 620$ , while using a light-jet mistagging efficiency  $\epsilon_{\text{mistag}} = 0.01$  and excluding the  $b$ -jet from the reconstructed hadronic top one would naively expect a much stronger suppression factor  $[n(n-1)/2 \epsilon_{\text{mistag}}^2 \epsilon_b]^{-1} \simeq 2400$  for an average number of light jets  $n = 4$ . However, there is a probability of about 7% that one  $b$ -quark escapes the hadronic top reconstruction (see topology  $A_3$  in Tab. III). In this case a single mistag is sufficient in order to arrive at three  $b$ -tags, and the corresponding suppression factor  $(0.07 n \epsilon_{\text{mistag}} \epsilon_b^2)^{-1} \simeq 730$  for  $n = 4$  is well consistent with the observed drop in  $t\bar{t}+\text{jets}$ . These considerations indicate that the signal and background cross sections after three  $b$ -tags are very sensitive to the details of  $b$ - and top-tagging, and to multi-jet emissions in the  $t\bar{t} + X$  background. The changes in  $S/B$  with respect to the original analysis of [7] can thus be attributed to the various modifications relative to these three aspects. We also note that an optimal suppression of the  $t\bar{t}+\text{jets}$  background could be easily achieved by requiring a fourth  $b$ -tag.

Concerning the differences between the HEPTopTagger used in the present analysis and the top tagging method employed in [7], the results presented in Sec. III A demonstrate that the HEPTopTagger efficiency is very robust irrespective of the pollution within the fat jet. In contrast, the tagger used in [7] has higher efficiency and light QCD jet mistag rate when a fat jet contains more hard radiation than only the top decay products. On the one hand, in general this can reduce  $S/B$ . But on the other hand the tagger used in [7] has a slightly higher overall efficiency as compared to the HEPTopTagger's efficiency of about 40%. For top-rich backgrounds this has no direct influence on  $S/B$ , but it can improve the statistical sensitivity of the analysis.

The sensitivity of the standard boosted analysis of Sec. III are displayed in Fig. 15a. For the scenario of a constant systematic uncertainty of 15% we find no sensitivity to modifications of the signal strength of  $|\mu| \lesssim 1$  at  $\mathcal{L} = 3000 \text{ fb}^{-1}$ . Hence, one can only exclude deviations from the Standard Model that are at least as large as the  $t\bar{t}H$  contribution it predicts. In Fig. 15 we see that this limit remains almost constant for integrated luminosities expected at the end of the following two LHC runs, suggesting the analysis will be dominated by the systematic uncertainty. In the more optimistic scenario presented in Fig. 16, where the systematic uncertainty scales as  $1/\sqrt{\mathcal{L}}$ , a limit around  $|\mu| = 0.5$  could be achieved at  $\mathcal{L} = 3000 \text{ fb}^{-1}$ .

## B. Improved boosted analyses T1–T5 and unboosted MVA approach

We now turn to the results of the boosted and unboosted analyses of Section IV. The evolution of signal and background cross sections at subsequent stages of the improved boosted analyses **T1–T5** and of the unboosted MVA analysis is presented in Table VI. The **T1** selection provides the sharpest signal peak and allows one to increase  $S/B$  after  $m_c$ -cut from 14%—in the case of a standard boosted analysis with **T1** and **T2** contributions—up to about 23%. This gain in sensitivity comes at a high price for the signal yield, as the **T1** topology is suppressed by roughly a factor four with respect to the complementary **T2** contribution. However, an extra ellipticity cut,  $\hat{t} < 0.2$ , can further increase  $S/B$  to 27% with only a 15% loss in the **T1** signal yield. At  $300 \text{ fb}^{-1}$  of integrated luminosity the expected number of  $t\bar{t}H$  events in the **T1** signal region is only twelve, but the higher  $S/B$  level for this topology results in an improved exclusion limit around  $|\mu| = 0.7$  at  $\mathcal{L} = 3000 \text{ fb}^{-1}$  (see Fig. 15). To increase the signal yield and accumulate sensitivity from other regions of the phase space, the **T1** selection can be combined with four statistically independent

Analysis	stage	$t\bar{t}H$	$t\bar{t}b\bar{b}$	$t\bar{t}+\text{jets}$	$t\bar{t}Z$	$S/B$
<b>T1</b>	before $b$ -tag	1.1	27	690	0.43	$1.5 \times 10^{-3}$
	3 $b$ -tags	0.075	0.77	0.37	0.032	0.064
	$m_c$ cut	0.042	0.13	0.053	$2.0 \times 10^{-3}$	0.23
	$\hat{t}$ cut	0.035	0.089	0.038	$9.5 \times 10^{-4}$	0.27
<b>T2</b>	before $b$ -tag	12	240	$4.6 \times 10^3$	4.5	$2.5 \times 10^{-3}$
	3 $b$ -tags	0.25	3.0	1.5	0.11	0.054
	$m_c$ cut	0.14	0.66	0.36	0.01	0.13
	$v_{\text{BDT}}$ cut	0.044	0.18	0.1	0.0031	0.15
<b>T3</b>	before $b$ -tag	51	$1.2 \times 10^3$	$1.9 \times 10^4$	18	$3.0 \times 10^{-3}$
	3 $b$ -tags	1.0	17	11	0.48	0.04
	$m_c$ cut	0.53	3.2	2.0	0.032	0.1
<b>T4</b>	before $b$ -tag	630	$1.5 \times 10^4$	$2.2 \times 10^5$	210	$3.0 \times 10^{-3}$
	3 $b$ -tags	5.6	130	92	2.2	0.02
	$m_c$ cut	1.5	16	10	0.2	0.06
<b>T5</b>	before $b$ -tag	4.2	220	$5.7 \times 10^3$	1.5	$7 \times 10^{-4}$
	3 $b$ -tags	0.14	1.6	0.65	0.036	0.06
	$m_c$ cut	0.094	0.6	0.28	0.011	0.11
MVA	>5 jets	14	420	$6.0 \times 10^3$	5.1	$2.2 \times 10^{-3}$
	4 $b$ -jets	1.5	19	2.9	0.52	0.066
	$v_{\text{BDT}}$ cut	0.041	0.16	0.033	$2.4 \times 10^{-3}$	0.21

TABLE VI: Signal and background cross sections in femtobarn and  $S/B$  ratios at different stages of the various boosted analyses (**T1**–**T5**) of Section IV A and for the unboosted MVA analysis of Section IV B.

channels: **T2**–**T5**.

In the **T2** channel, with three Higgs candidates in a fat jet, we are able to improve  $S/B$  from 13% (after  $m_c$  cut) to 15% by applying a BDT made of 5 variables that define the reconstructed  $t\bar{t}H$  system, as discussed in Sec. IV A 1. However, the  $v_{\text{BDT}}$  cut suppresses the signal by about a factor three. Moreover, several of the attempted modifications, e.g. cutting on  $\chi^2$ , using the jet shape observable ellipticity, and exploiting the angle between the leptonic top's  $b$ -quark and lepton, do not improve  $S/B$ . Nevertheless, combining **T1** and **T2** without the aforementioned modifications in the CLs does improve the limit from  $|\mu| \simeq 0.7$  to  $|\mu| \simeq 0.6$ .

The topologies **T3**–**T5**, which contain at least one boosted resonance, feature  $S/B$  ratios from 6% to 11%, and a factor eleven more signal cross section than the **T1**–**T2** selections. The inclusion of all five channels in the CL calculation allows one to exclude  $|\mu| \gtrsim 0.45$ .

Finally, let us consider the analysis of Section IV B, which entirely relies on a BDT without requiring the presence of a fat jet in the final state. This channel is not independent from **T1**–**T5** and is closer in spirit to analyses performed by ATLAS and CMS during Run 1. In Table VI we present results for a fairly tight cut on the  $v_{\text{BDT}}$  discriminant, which is chosen in such a way that the resulting signal yield is the same as for the individual boosted selection with the highest discriminating power, i.e. **T1**. In this case the BDT analysis reaches  $S/B \simeq 21\%$ , which lies slightly below the result of the **T1** selection (23% without  $\hat{t}$  cut). With a looser  $v_{\text{BDT}}$  cut it is possible to increase the signal yield by an order of magnitude while keeping  $S/B \simeq 18\%$ . For the scenario of 15% systematic background uncertainty we find that exploiting the full distribution of  $v_{\text{BDT}}$  in the profiled likelihood method permits to exclude  $|\mu| \gtrsim 0.55$  at  $\mathcal{L} = 3000 \text{ fb}^{-1}$ . Thus the BDT limit lies between the results of the **T1** analysis ( $|\mu| \simeq 0.7$ ) and the combination of **T1**–**T5** ( $|\mu| \simeq 0.45$ ). However, when comparing boosted and BDT selections, one should keep in mind that the emergence of a Higgs peak in the  $m_c$  distribution represents a key added value of the **T1** analysis, as it permits to use a side-band approach in order to mitigate theoretical uncertainties in the shapes of the  $t\bar{t} + X$  backgrounds. Moreover the presence of a measurable  $Z \rightarrow b\bar{b}$  peak provides extra opportunities for a further reduction of the systematic uncertainties.

It will take the LHC more than a decade to collect  $3000 \text{ fb}^{-1}$ , thus we expect significant improvements in the systematic uncertainties of  $t\bar{t} + X$  final states. Thus in Fig. 16 we present a more optimistic scenario, where above  $\mathcal{L} = 300 \text{ fb}^{-1}$  the background systematic uncertainty starts decreasing below 15% and scales inversely proportionally to the square root of the integrated luminosity. For shrinking uncertainties, equally applied to all channels, the final signal yield becomes of crucial importance. Therefore individual boosted channels cannot compete with the unboosted analysis in setting a limit for  $\mu$ . The **T1** topology alone can exclude deviations larger than 50% of the expected null

hypothesis, while the unboosted BDT analysis achieves 29%. The combination of all five boosted topologies however, still offers the best exclusion limit at  $|\mu| \gtrsim 0.26$ . This limit can be further improved by including  $b$ -jet energy correction as discussed in Sec. V. When neutrinos from hadronic decays are used in the reconstruction, the combination of the **T1–T5** analyses yields the limit  $|\mu| = 0.2$ .

## VII. SUMMARY AND CONCLUSIONS

We have re-evaluated LHC’s potential to set a limit on the signal strength  $\mu$  in the semi-leptonic  $t\bar{t}H(b\bar{b})$  channel. We first focused on events with simultaneously moderately boosted Higgs boson and hadronic top quark. This channel was proposed earlier to discover a light Higgs boson [7] and was expected to provide a good handle in measuring  $\mu$ . After improving on the simulation of signal and backgrounds and applying a more conservative particle identification, we find that achieving a sensitivity to small deviations in  $\mu$  is more challenging than anticipated. Therefore, to increase the sensitivity, we split the  $t\bar{t}H$  phase space into several independent regions and combined their individual contributions. In particular, we extended the search into new phase space regions, where only one of the hadronically decaying resonances is boosted. These improvements allow us to dramatically reduce the 95% CL limit from  $|\mu| = 1.0$  to  $|\mu| = 0.2$  for  $3\text{ab}^{-1}$  of integrated luminosity. We acknowledge the previous statement is very dependent on the handling of both theoretical uncertainties in the normalisation and shape of the  $t\bar{t} + X$  distributions and systematic effects in the experimental reconstruction of particles. Therefore, we encourage theoretical and experimental studies of the boosted channels in  $t\bar{t} + X$  events in order to make use of the full phase space accessible at the LHC.

## Acknowledgments

We thank A. Denner, S. Dittmaier and L. Hofer for providing us with the one-loop tensor-integral library COLLIER and F. Krauss for collaboration during early stages of this work. This research was supported in part by the Swiss National Science Foundation (SNF) under contract PP00P2-153027 and by the Research Executive Agency (REA) of the European Union under the Grant Agreements PITN-GA-2012-315877 (*MCnet*) and PITN-GA-2012-316704 (*HiggsTools*).

- 
- [1] G. Aad et al. (ATLAS), Phys. Lett. **B716**, 1 (2013), 1207.7214.
  - [2] S. Chatrchyan et al. (CMS), Phys. Lett. **B716**, 30 (2013), 1207.7235.
  - [3] T. ATLAS and C. Collaborations (2015).
  - [4] R. Lafaye, T. Plehn, M. Rauch, D. Zerwas, and M. Duhrssen, JHEP **08**, 009 (2009), 0904.3866.
  - [5] J. M. Butterworth, A. R. Davison, M. Rubin, and G. P. Salam, Phys. Rev. Lett. **100**, 242001 (2008), 0802.2470.
  - [6] D. E. Soper and M. Spannowsky, JHEP **08**, 029 (2010), 1005.0417.
  - [7] T. Plehn, G. P. Salam, and M. Spannowsky, Phys. Rev. Lett. **104**, 111801 (2010), 0910.5472.
  - [8] G. T. Bodwin, F. Petriello, S. Stoynev, and M. Velasco, Phys. Rev. **D88**, 053003 (2013), 1306.5770.
  - [9] A. L. Kagan, G. Perez, F. Petriello, Y. Soreq, S. Stoynev, and J. Zupan, Phys. Rev. Lett. **114**, 101802 (2015), 1406.1722.
  - [10] M. König and M. Neubert, JHEP **08**, 012 (2015), 1505.03870.
  - [11] G. Degrossi, S. Di Vita, J. Elias-Miro, J. R. Espinosa, G. F. Giudice, G. Isidori, and A. Strumia, JHEP **08**, 098 (2012), 1205.6497.
  - [12] D. Buttazzo, G. Degrossi, P. P. Giardino, G. F. Giudice, F. Sala, A. Salvio, and A. Strumia, JHEP **12**, 089 (2013), 1307.3536.
  - [13] F. Demartin, F. Maltoni, K. Mawatari, and M. Zaro, Eur. Phys. J. **C75**, 267 (2015), 1504.00611.
  - [14] S. Frixione, V. Hirschi, D. Pagani, H. S. Shao, and M. Zaro, JHEP **06**, 184 (2015), 1504.03446.
  - [15] S. Dawson, L. H. Orr, L. Reina, and D. Wackerroth, Phys. Rev. **D67**, 071503 (2003), hep-ph/0211438.
  - [16] W. Beenakker, S. Dittmaier, M. Kramer, B. Plumper, M. Spira, and P. M. Zerwas, Phys. Rev. Lett. **87**, 201805 (2001), hep-ph/0107081.
  - [17] M. R. Buckley and D. Goncalves (2015), 1507.07926.
  - [18] M. Casolino, T. Farooque, A. Juste, T. Liu, and M. Spannowsky (2015), 1507.07004.
  - [19] H.-L. Li, P.-C. Lu, Z.-G. Si, and Y. Wang (2015), 1508.06416.
  - [20] S. Amor dos Santos et al., Phys. Rev. **D92**, 034021 (2015), 1503.07787.
  - [21] K. Kolodziej and A. Slapik, Eur. Phys. J. **C75**, 475 (2015), 1507.01572.
  - [22] J. Ellis, D. S. Hwang, K. Sakurai, and M. Takeuchi, JHEP **04**, 004 (2014), 1312.5736.
  - [23] J. Yue, Phys. Lett. **B744**, 131 (2015), 1410.2701.
  - [24] M. Farina, C. Grojean, F. Maltoni, E. Salvioni, and A. Thamm, JHEP **05**, 022 (2013), 1211.3736.

- [25] C. Degrande, J. M. Gerard, C. Grojean, F. Maltoni, and G. Servant, JHEP **07**, 036 (2012), [Erratum: JHEP03,032(2013)], 1205.1065.
- [26] C. Englert and E. Re, Phys. Rev. **D89**, 073020 (2014), 1402.0445.
- [27] G. Aad et al. (ATLAS), Phys. Lett. **B749**, 519 (2015), 1506.05988.
- [28] G. Aad et al. (ATLAS), Phys. Lett. **B740**, 222 (2015), 1409.3122.
- [29] V. Khachatryan et al. (CMS), JHEP **09**, 087 (2014), [Erratum: JHEP10,106(2014)], 1408.1682.
- [30] F. Maltoni, D. L. Rainwater, and S. Willenbrock, Phys. Rev. **D66**, 034022 (2002), hep-ph/0202205.
- [31] A. Belyaev and L. Reina, JHEP **08**, 041 (2002), hep-ph/0205270.
- [32] D. Curtin, J. Galloway, and J. G. Wacker, Phys. Rev. **D88**, 093006 (2013), 1306.5695.
- [33] N. Craig, M. Park, and J. Shelton (2013), 1308.0845.
- [34] C. Buttar et al., in *Physics at TeV colliders. Proceedings, Workshop, Les Houches, France, May 2-20, 2005* (2006), hep-ph/0604120.
- [35] P. Artoisenet, P. de Aquino, F. Maltoni, and O. Mattelaer, Phys. Rev. Lett. **111**, 091802 (2013), 1304.6414.
- [36] G. Aad et al. (ATLAS), Eur. Phys. J. **C75**, 349 (2015), 1503.05066.
- [37] V. Khachatryan et al. (CMS), Eur. Phys. J. **C75**, 251 (2015), 1502.02485.
- [38] X.-G. He, G.-N. Li, and Y.-J. Zheng, Int. J. Mod. Phys. **A30**, 1550156 (2015), 1501.00012.
- [39] M. L. Mangano, T. Plehn, P. Reimitz, T. Schell, and H.-S. Shao (2015), 1507.08169.
- [40] T. Gleisberg, S. Höche, F. Krauss, M. Schönherr, S. Schumann, F. Siegert, and J. Winter, JHEP **02**, 007 (2009), 0811.4622.
- [41] S. Schumann and F. Krauss, JHEP **03**, 038 (2008), 0709.1027.
- [42] T. Gleisberg and F. Krauss, Eur. Phys. J. **C53**, 501 (2008), 0709.2881.
- [43] T. Gleisberg and S. Höche, JHEP **12**, 039 (2008), 0808.3674.
- [44] F. Cascioli, P. Maierhöfer, and S. Pozzorini, Phys. Rev. Lett. **108**, 111601 (2012), 1111.5206.
- [45] F. Cascioli, J. Lindert, P. Maierhöfer, and S. Pozzorini, *The OPENLOOPS one-loop generator*, URL <http://openloops.hepforge.org>.
- [46] A. Denner, S. Dittmaier, and L. Hofer, PoS **LL2014**, 071 (2014), 1407.0087.
- [47] A. Denner and S. Dittmaier, Nucl. Phys. **B734**, 62 (2006), hep-ph/0509141.
- [48] A. Denner and S. Dittmaier, Nucl. Phys. **B844**, 199 (2011), 1005.2076.
- [49] P. Richardson, JHEP **11**, 029 (2001), hep-ph/0110108.
- [50] S. Höche, S. Kuttimalai, S. Schumann, and F. Siegert, Eur. Phys. J. **C75**, 135 (2015), 1412.6478.
- [51] H.-L. Lai, M. Guzzi, J. Huston, Z. Li, P. M. Nadolsky, J. Pumplin, and C. P. Yuan, Phys. Rev. **D82**, 074024 (2010), 1007.2241.
- [52] J. R. Andersen et al. (LHC Higgs Cross Section Working Group) (2013), 1307.1347.
- [53] S. Höche, F. Krauss, M. Schönherr, and F. Siegert, JHEP **09**, 049 (2012), 1111.1220.
- [54] S. Höche, F. Krauss, M. Schönherr, and F. Siegert, Phys. Rev. Lett. **110**, 052001 (2013), 1201.5882.
- [55] S. Frixione and B. R. Webber, JHEP **06**, 029 (2002), hep-ph/0204244.
- [56] F. Cascioli, P. Maierhöfer, N. Moretti, S. Pozzorini, and F. Siegert, Phys. Lett. **B734**, 210 (2014), 1309.5912.
- [57] S. Höche, F. Krauss, M. Schönherr, and F. Siegert, JHEP **04**, 027 (2013), 1207.5030.
- [58] T. Gehrmann, S. Höche, F. Krauss, M. Schönherr, and F. Siegert, JHEP **01**, 144 (2013), 1207.5031.
- [59] R. Frederix and S. Frixione, JHEP **12**, 061 (2012), 1209.6215.
- [60] S. Höche, J. Huang, G. Luisoni, M. Schönherr, and J. Winter, Phys. Rev. **D88**, 014040 (2013), 1306.2703.
- [61] S. Höche, F. Krauss, P. Maierhöfer, S. Pozzorini, M. Schönherr, and F. Siegert, Phys. Lett. **B748**, 74 (2015), 1402.6293.
- [62] K. Melnikov and M. Schulze, Nucl. Phys. **B840**, 129 (2010), 1004.3284.
- [63] G. Bevilacqua, M. Czakon, C. G. Papadopoulos, and M. Worek, Phys. Rev. Lett. **104**, 162002 (2010), 1002.4009.
- [64] M. Czakon, P. Fiedler, and A. Mitov, Phys. Rev. Lett. **110**, 252004 (2013), 1303.6254.
- [65] T. Plehn, M. Spannowsky, M. Takeuchi, and D. Zerwas, JHEP **10**, 078 (2010), 1006.2833.
- [66] Y. L. Dokshitzer, G. D. Leder, S. Moretti, and B. R. Webber, JHEP **08**, 001 (1997), hep-ph/9707323.
- [67] W. Bartel et al. (JADE), Phys. Lett. **B123**, 460 (1983).
- [68] F. Krauss, P. Petrov, M. Schönherr, and M. Spannowsky, Phys. Rev. **D89**, 114006 (2014), 1403.4788.
- [69] D. E. Kaplan, K. Rehermann, M. D. Schwartz, and B. Tweedie, Phys. Rev. Lett. **101**, 142001 (2008), 0806.0848.
- [70] P. Speckmayer, A. Hocker, J. Stelzer, and H. Voss, J. Phys. Conf. Ser. **219**, 032057 (2010).
- [71] I. Antcheva et al., Comput. Phys. Commun. **182**, 1384 (2011).
- [72] L. Moneta, K. Belasco, K. S. Cranmer, S. Kreiss, A. Lazzaro, D. Piparo, G. Schott, W. Verkerke, and M. Wolf, PoS **ACAT2010**, 057 (2010), 1009.1003.